Journal of Controlled Release 394 (2026) 114863

Contents lists available at ScienceDirect

Journal of Controlled Release

journal homepage: www.elsevier.com/locate/jconrel

Toward animal-free approaches in subcutaneous drug delivery: A pain management case study

Remo Eugster [a], Niklaas Manten [a], Giorgio Buttitta [b], Götz Chwatal [c], Stefan Schürch [a], Alessandra Bergadano [d], Simone Aleandri [a], Paola Luciani [a,*]

[a] Department of Chemistry, Biochemistry and Pharmaceutical Sciences, University of Bern, Bern, Switzerland
[b] Department of Drug Chemistry and Technologies, Sapienza University of Rome, Rome, Lazio, Italy
[c] Institute of Animal Pathology, Vetsuisse Faculty, University of Bern, Bern, Switzerland
[d] Experimental Animal Center (EAC), University of Bern, Bern, Switzerland

ARTICLE INFO

Keywords:
Liposomal depots
3R
Long-acting injectables
Subcutaneous administration
IVIVC
Machine learning
Pharmacokinetics

ABSTRACT

Subcutaneous (s.c.) administration offers practical advantages for long-acting drug delivery, yet its complex tissue environment, lack of standardized models, and limited regulatory guidance pose challenges for predicting pharmacokinetics (PK). Here, we present a complementary set of experimental and computational approaches to reduce reliance on animal testing while maintaining translational relevance. Ex vivo skin models captured the influence of tissue variability, while 3D-printed constructs and molded agarose hydrogels enabled standardized, reproducible in vitro drug release studies. In parallel, machine learning models trained on curated rodent datasets predicted key PK parameters with strong agreement to in vivo data, providing an alternative that bypasses additional animal experiments and resource-intensive assays. Finally, a liposomal carprofen formulation case study demonstrated the translational potential of these methods in veterinary applications. Together, these strategies illustrate routes toward animal-free drug development: simplified experimental systems that mimic s.c. release and computational models that predict systemic PK. By combining them conceptually, we outline a framework that advances the 3Rs principles while supporting mechanistic and predictive understanding of s.c. drug delivery.

1. Introduction

The evolving therapeutic landscape, driven by the rise of biologics, long-acting formulations, and treatments for chronic diseases, increasingly demands delivery routes that can provide reliable systemic exposure outside clinical settings [1]. In this context, the subcutaneous (s.c.) space has emerged as a particularly attractive site, offering the possibility to deliver large molecules, sustain drug release, and enable dosing regimens compatible with long-term therapy [1,2]. Beyond these therapeutic drivers, s.c. administration also provides practical advantages such as patient-centric self-administration, avoidance of first-pass metabolism, and the potential for sustained pharmacological effects [2].

At the same time, the s.c. space represents a structurally heterogeneous and biologically active environment composed of adipose tissue, extracellular matrix networks, fibroblasts, vasculature, and lymphatic drainage pathways [1]. Importantly, the s.c. space is not a static acceptor organ but a dynamic and compartmentalized tissue environment. The interplay between extracellular matrix architecture, adipose lobules, capillary and lymphatic networks, and interstitial fluid transport governs local drug retention, depot dispersal, and systemic uptake [3,4]. These processes are further modulated by tissue perfusion, enzymatic activity, local inflammatory status, and species- or site-dependent anatomical differences, which together contribute to substantial variability in s.c. pharmacokinetics and formulation performance across in vivo settings [1,3,4]. These elements collectively govern depot formation, local drug retention, lymphatic drainage, interstitial fluid transport, and systemic uptake, leading to high variability in pharmacokinetics and tissue response across compounds and formulations [1]. This complexity poses a particular challenge for the development and evaluation of long-acting injectables, where both the rate of absorption and the persistence of the depot critically determine therapeutic performance [1,5].

Pain management provides a particularly relevant application context in this regard. Analgesics are frequently administered s.c. in

---

* Corresponding author.
E-mail address: paola.luciani@unibe.ch (P. Luciani).

https://doi.org/10.1016/j.jconrel.2026.114863
Received 4 November 2025; Received in revised form 11 March 2026; Accepted 24 March 2026
Available online 26 March 2026

both human and veterinary settings, where repeated dosing can induce additional stress, handling-related discomfort, and welfare concerns [6–8]. Long-acting s.c. formulations are therefore highly desirable, as they can extend the duration of analgesia while reducing intervention frequency [6,7]. However, the development and assessment of such formulations still rely largely on in vivo testing, owing to the lack of standardized models that adequately reproduce the complexity of the s.c. tissue environment [7].

Consequently, progress in developing long-acting injectables for s.c. administration has been hampered by the absence of reliable in vitro models that manage to capture the complexity of the s.c. space [9,10]. Pharmacokinetics (PK) and formulation performance are still predominantly assessed in animal models, which, while informative, are resource-intensive and raise ethical concerns due to repeated injections and associated discomfort [11,12]. In line with the 3R principles (Replacement, Reduction, Refinement), there is growing pressure to minimize animal use without compromising scientific rigor. Refinement strategies, such as formulation approaches that reduce dosing frequency, can already alleviate animal distress, but broader innovations are required to reduce reliance on animal experiments further [8,13–15].

In parallel, a strong shift toward new approach methodologies is underway, with the U.S. Food and Drug Administration (FDA) no longer explicitly requiring animal experiments for some drug classes [16,17]. Ex vivo tissue models, engineered artificial constructs, and computational tools are being developed to capture the complex environment of the s.c. space in controlled laboratory settings [18–21]. Each of these approaches offers unique opportunities: ex vivo models maintain native tissue complexity, artificial tissues enable standardization and reproducibility, and computational methods allow for rapid exploration of PK behavior [18–21]. At the same time, limitations remain: ex vivo systems still rely on animal-derived material, engineered constructs often require specialized infrastructure, and computational models are highly dependent on the quality and diversity of training data [18,22]. Also, the complexity of the s.c. space itself, which combines extracellular matrix, adipose tissue, vasculature, and lymphatic networks, bears great challenges in implementation [1,4,21].

Among computational approaches, machine learning (ML) has emerged as a powerful tool for predicting pharmacokinetics [22,23]. Numerous ML-based PK models exist, but they predominantly focus on oral or intravenous administration and are designed for human applications [23]. In contrast, robust ML models for laboratory animals are rare, yet highly relevant: they could guide experimental design, improve planning of in vivo studies, and help reduce animal numbers in line with the 3Rs [13,24–26].

Here, we explore a set of complementary methods to investigate s.c. drug administration. Our approach integrates ex vivo testing, artificial tissue constructs, and hydrogel-based in vitro systems with ML-based PK predictions. Together, these methods aim to provide a balanced framework that reduces reliance on animal testing while retaining mechanistic and translational insight. Beyond simply showcasing these complementary methods, our study provides for the first time a comparative perspective on their respective advantages and limitations, which may guide the scientific community toward greater standardization or at least facilitate the selection of the most suitable tools for specific research needs. However, it is important to note that the approaches investigated in this work do not aim to recreate the full structural and physiological complexity of the s.c. tissue environment. Rather, each strategy encompasses selected aspects of the underlying processes to enable controlled, reproducible investigation of factors that are otherwise difficult to disentangle in vivo. Finally, we illustrate the translational potential of these strategies through a case study on a liposomal carprofen formulation, highlighting their application in veterinary medicine.

2. Results and discussion

2.1. Ex vivo models

A key limitation of s.c. ex vivo models lies in their variability [27,28]. Skin samples may differ considerably depending on their origin, including the conditions under which the donor animal was raised (e.g., size, age, diet) and the institution (e.g. abattoir) where the tissue was collected [28–30]. Additional factors, such as anatomical site and inter-animal variability, can further influence tissue properties [28,31]. We recently demonstrated the use of porcine skin disks in an ex vivo dialysis setup to evaluate the release of bupivacaine, a widely used local anesthetic, following injection into the tissue and thereby bridging this gap to mimic the s.c. space [18]. To assess the variability of such ex vivo models, here we sourced different porcine skin samples and injected them with chemical grade bupivacaine solution. Fig. 1 illustrates how the aforementioned factors affect drug release profiles from skin samples. The origin of the skin was found to exert a pronounced effect, suggesting that broader biological factors - such as animal physiology and pre-slaughter conditions can significantly alter tissue permeability and drug diffusion [31]. In contrast, no statistically significant differences were observed between abdominal and cervical skin, nor across animals of the same subspecies, suggesting that regional skin composition and moderate inter-animal variability are less critical for short-term release behavior [31].

Together, these findings highlight an important caveat of traditional ex vivo methods: reproducibility depends strongly on tissue sourcing, making results difficult to generalize [28]. While skin disks offer a convenient means of approximating s.c. drug release, the inherent variability raises questions about their reliability for systematic formulation development. Further, while no animal license is required, one should acknowledge the ethical consideration that the tissue source still depends on animal sacrifice [28]. This motivates the exploration of alternative systems that combine biological relevance with reduced variability and greater experimental control.

2.2. 3D-printed artificial tissue

To minimize the variability of freshly excised tissue with heterogeneous origins, we engineered a skin-derived ink for 3D printing standardized artificial tissue models, suitable for studying drug release after s.c. administration [32–34]. Beyond pharmaceutical testing, 3D printing has already established a strong foothold in drug and formulation development, enabling precise control over dosage forms, release kinetics, and personalized therapies [35–40]. In the biomedical field, efforts have focused on bioprinting artificial skin for wound healing and burn treatment, demonstrating the potential of printed tissues to mimic complex biological structures [33,41,42]. However, despite these advances, the use of 3D-printed skin models for drug release studies still remains a niche application [43]. This highlights both the novelty and the significance of developing reproducible printed tissues as in vitro testbeds for subcutaneous formulations [43]. While bioink systems incorporating dermal or ECM-derived components for skin reconstruction have been previously reported, [42] our approach differs in scope and intent. Instead of aiming at anatomical or regenerative fidelity, the construct is parameterized as a functional, reproducible test platform for assessing injectability, drug release, and depot accommodation under controlled conditions.

To realize such a system, isolated skin components were homogenized and processed into porcine skin powder (PSP), which was then blended with alginate (ALG) for cohesiveness and hydroxypropylmethylcellulose (HPMC) as a thickener [44,45]. Cross-linking stabilized the matrix, yielding constructs with structural integrity while retaining sufficient porosity to allow drug injection without reflux - an issue often encountered with overly elastic or dense hydrogel systems (Fig. 2A) [44]. Accordingly, the innovation of this construct lies in

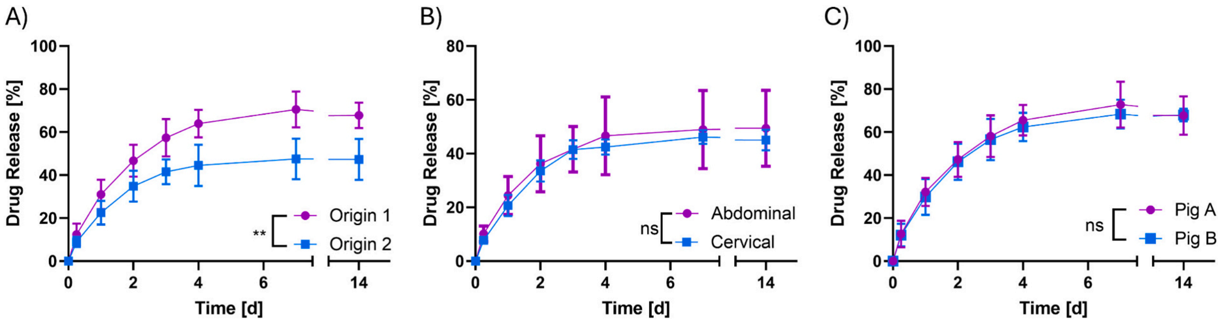

Fig. 1. Comparative ex vivo release profiles of bupivacaine from skin samples of varying sources. A) Influence of tissue origin, B) differences between abdominal and cervical skin while keeping animal origin constant, and C) inter-animal variability while keeping origin of sourcing and anatomical tissue sample constant. A two-way ANOVA with the factors "time" and "tissue origin" was performed, where origin showed a significant main effect.

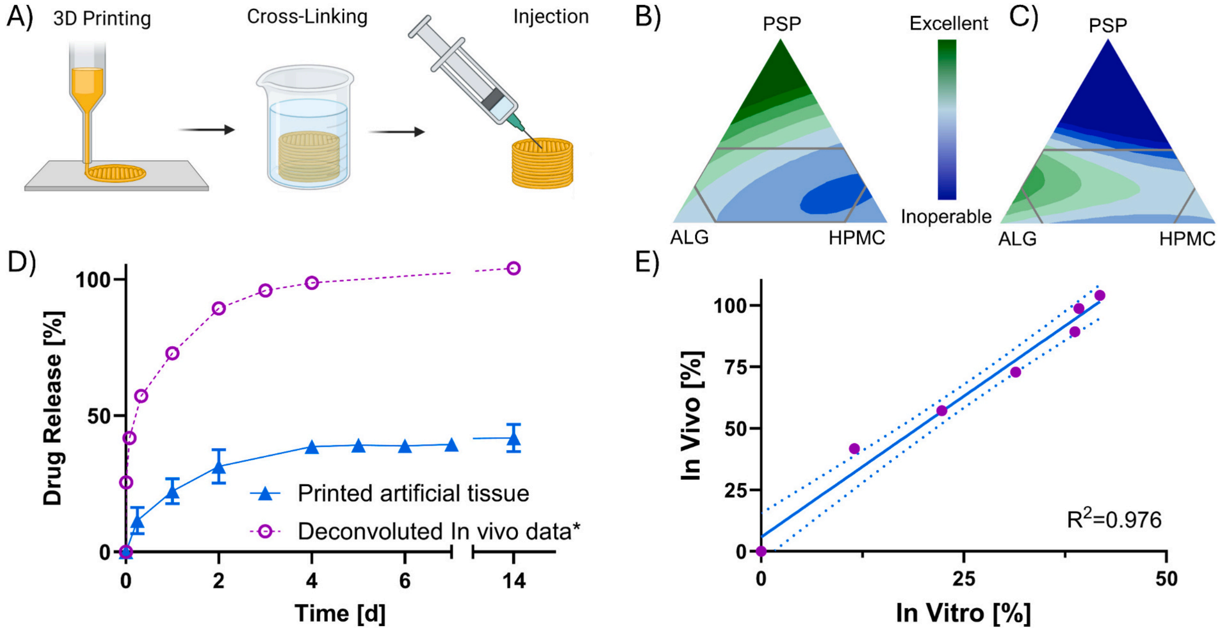

Fig. 2. Development and application of 3D-printed artificial tissue for in vitro drug release studies. A) Fabrication process using additive manufacturing, B) DoE-derived contour plot of ink printability based on PSP, ALG, and HPMC. The optimal region lies toward the vertices of the mixture triangle, reflecting the requirement for substantial PSP to mimic s.c. tissue, C) DoE-derived contour plot of injectability. Together with panel B, these plots illustrate the two independent readouts (printability and injectability) used for optimization. By overlaying both responses, a compromise formulation was selected (PSP 9%, ALG 12.5%, HPMC 5%, buffer 63.5%). D) Cumulative release profile of bupivacaine from printed artificial tissue and *deconvoluted in vivo data from Aleandri et al.[13]. E) Scatter plot showing correlation between convoluted in vivo release (derived from PK assuming full bioavailability) and in vitro release, with regression line and 90% confidence interval. Note that, while the raw in vivo and in vitro curves (panel D) do not align directly, transformation into cumulative release allows meaningful comparison, yielding a strong linear relationship ($R^2 = 0.976$).

its application context to capture drug release properties that are otherwise difficult to isolate in vivo. To systematically design and optimize the skin ink, a design of experiments (DoE) methodology was applied. DoE is a cornerstone of modern pharmaceutical development, enabling systematic exploration of formulation and process parameters within a defined design space [35,38,46,47]. By replacing trial-and-error with predefined objectives and quality risk management, it ensures reliable and reproducible outcomes [46,48]. The study investigated four material attributes (PSP, ALG, HPMC, and buffer) and two process parameters (printing speed and pressure) to assess their impact on two quality attributes (injectability and printability) [38]. The design space was chosen deliberately to accommodate significant proportions of PSP, ensuring that the final tissue mimicked essential aspects of the s.c. space (details of parameters and rating scales can be found in the Supporting Information) of the mixture triangle, reflecting the requirement for substantial PSP to mimic s.c. tissue, C) DoE-derived contour plot of injectability. Together with panel B, these plots illustrate the two independent readouts (printability and injectability) used for optimization. By overlaying both responses, a compromise formulation was selected (PSP 9%, ALG 12.5%, HPMC 5%, buffer 63.5%). D) Cumulative release profile of bupivacaine from printed artificial tissue and *deconvoluted in vivo data from Aleandri et al. [18]. E) Scatter plot showing correlation between convoluted in vivo release (derived from PK assuming full bioavailability) and in vitro release, with regression line and 90% confidence interval. Note that, while the raw in vivo and in vitro curves (panel D) do not align directly, transformation into cumulative release allows meaningful comparison, yielding a strong linear relationship ($R^2 = 0.976$).

The DoE analysis revealed distinct trade-offs. Printability increased with higher PSP content (Fig. 2B), likely because HPMC at elevated concentrations tended to clog the printing nozzle, limiting its effectiveness as a thickener. However, injectability showed the opposite trend: high PSP or HPMC levels resulted in systems that were unsuitable for drug delivery. Excessive HPMC produced gels that were too rigid, causing injected drugs either to reflux or fail to penetrate. In contrast, excessive PSP reduced structural cohesion, making it impossible to retain a 100 μL injection (Fig. 2C). Alginate proved critical in balancing these competing effects, as its gel-forming capacity provided cohesiveness while maintaining adequate flexibility [44,49,50]. By overlaying the responses and performing response optimization, the most favorable composition was identified: PSP 9%, ALG 12.5%, HPMC 5%, and buffer 63.5%. This optimized formulation produced a homogeneous bioink that could be reliably printed into skin-like tissues. After the DoE optimization, printing pressure was kept fixed at 90 kPa and the infill density at 20%; further, the printing speed was always kept at 10 mm/s.

These compositional effects can be rationalized by considering the microstructural roles of the individual components in the composite matrix. Alginate forms an ionically cross-linked network upon exposure to Ca^{2+}, providing the primary cohesive scaffold that stabilizes the printed architecture and preserves pore continuity [49,51]. In contrast, HPMC mainly contributes through polymer chain entanglement and hydration-induced swelling, which increases viscoelastic resistance and improves line definition during extrusion, but at higher fractions leads to dense, low-permeability domains that hinder needle penetration and promote reflux during injection [52,53]. PSP acts as a particulate filler derived from decellularized dermal tissue; at moderate contents, it enhances structural rigidity and mimics the granular character of native s.c. tissue, whereas excessive loading disrupts network integrity and reduces the matrix's capacity to accommodate an injected depot [45]. The observed injectability–printability trade-off in the DoE study therefore reflects the balance between network cohesion (ALG/PSP) and viscoelastic resistance (HPMC), which must remain sufficiently high to support printing while still allowing local matrix deformation during injection [54].

Beyond functional performance, the artificial tissues offered additional advantages over ex vivo disks. Most notably, the bioink could be stored at 4 °C and printed on demand, providing an extended shelf-life, whereas native skin samples had to be used immediately after excision. Using this system, homogeneous artificial tissue disks were printed and used to assess the release of bupivacaine at 37 °C under controlled conditions. The printed tissue yielded highly reproducible release profiles (Fig. 2D), but comparing it to in vivo PK data is crucial for its assessment; hence, data reported by Aleandri et al. was consulted [18]. Since in vitro diffusion profiles cannot be directly compared to plasma concentration-time curves, the PK data were convoluted into cumulative release curves, assuming complete bioavailability - a valid assumption for parenteral administration [55]. When plotted directly, the in vitro release profile of the printed tissue and the plasma concentration–time curve from in vivo studies did not overlap due to their inherently different readouts (drug released vs. plasma levels). To enable comparison, the in vivo PK data were convoluted into cumulative release curves, assuming complete bioavailability. This transformation allowed both datasets to be expressed on the same scale. When compared in this way, a strong linear correlation emerged ($R^2 = 0.976$; Fig. 2E), highlighting that although the curves do not visually match one-to-one, the overall release kinetics are well captured by the printed tissue system.

Several critical considerations remain, though. Specialized bioprinters are required, which may limit accessibility and scalability in routine pharmaceutical development [56]. Ink preparation itself is labor-intensive, and despite the reduction in variability compared to native skin, the approach still depends on animal-derived material, raising ethical concerns [28,45]. Also, as there is no active clearance, due to the fat present, lipophilic drugs might tend to remain in the system and therefore be poorly represented. Furthermore, sterilization of the constructs poses technical challenges, as the combination of biological and polymeric components is sensitive to conventional sterilization methods [57].

Overall, 3D-printed artificial skin models represent a promising step toward more reproducible in vitro testing of s.c. formulations [56]. They offer improved standardization, reproducibility, and flexibility over traditional ex vivo methods [27,44,56]. At the same time, their reliance on complex preparation steps and residual animal material highlights the need for even simpler, more sustainable alternatives.

2.3. *Molded hydrogel system*

While 3D-printed tissues offer reproducibility and biological relevance, simpler approaches may be more practical for routine testing and large-scale applications. One such method is the use of molded hydrogels as in vitro models for subcutaneous drug diffusion [58–60]. In this study, agarose hydrogels cast into cylindrical tubes were employed as a straightforward and sustainable surrogate for s.c. tissue. Their simplicity, low cost, and reproducibility make them an attractive option for early-stage screening [58–60].

To evaluate the robustness of the model, two drugs with distinct physicochemical properties were selected. Alongside bupivacaine, carprofen (Rimadyl®) – a nonsteroidal anti-inflammatory drug widely used in veterinary practice - was chosen as a more lipophilic counterpart. Including both compounds provided a meaningful comparison, as lipophilic drugs often display slower dissolution, precipitation tendencies, or prolonged persistence in lipophilic environments [59,61,62]. Interestingly, the agarose system yielded consistent release kinetics for both drugs (Fig. 3A). Carprofen diffused completely from the matrix, whereas bupivacaine reached only ~50% release. The latter likely reflects a stronger interaction of bupivacaine with the agarose matrix or partial sequestration due to its amphiphilic properties, rather than a shortcoming of the system itself [18].

S.c. injection of carprofen in rats produced a pharmacokinetic profile consistent with its clinical use: rapid systemic availability (<15 min) followed by a gradual decline over 24 h (Fig. 3B) [63]. This PK profile is consistent with reported in vivo data on carprofen's elimination half-life and dosing frequency in this species [63]. However, cumulative drug release from in vitro diffusion systems cannot be directly compared to plasma concentration–time profiles [55]. As previously described, to enable meaningful comparison, PK data were convoluted into cumulative release curves, assuming complete bioavailability - a valid assumption for parenteral administration [55]. This transformation places both datasets on the same scale, thereby revealing a strong linear relationship with the in vitro release profile ($R^2 = 0.898$; Fig. 3C and Supporting Information).

Closer inspection of the correlation showed that the in vitro system slightly underestimated release during the second quarter of the profile. This lag may be explained by structural constraints within the agarose gel, which can impede diffusion compared to the dynamic clearance and tissue perfusion occurring in vivo [55,58,64]. Nonetheless, the strong overall agreement highlights the potential of this simple hydrogel model to approximate in vivo release kinetics with good fidelity [55].

Nevertheless, it needs to be pointed out that the discussed models so far necessarily represent simplified abstractions of the s.c. space, as they lack active clearance, perfusion, and the dynamic remodeling that occurs in vivo. Their value therefore lies not in anatomical fidelity, but in providing mechanistic insight under well-controlled conditions, which can inform formulation screening, hypothesis generation, and the refinement of subsequent in vivo studies in line with the 3R principles.

In hydrogel-based systems, the apparent diffusion kinetics are influenced by parameters such as agarose concentration, gel rigidity, and the effective diffusion path length defined by the cavity geometry [58–60]. Higher agarose contents decrease mesh size and increase tortuosity, thereby slowing the apparent release rate, whereas lower concentrations produce more permissive matrices with faster diffusion [58]. As previously discussed for diffusion-controlled release from parenteral depots, including PLGA-based systems [65], such in vitro configurations are particularly suitable for comparing cumulative release behavior under standardized conditions. In the present study, the chosen agarose concentration and gel dimensions were selected as a compromise between structural stability and a diffusional resistance that approximates

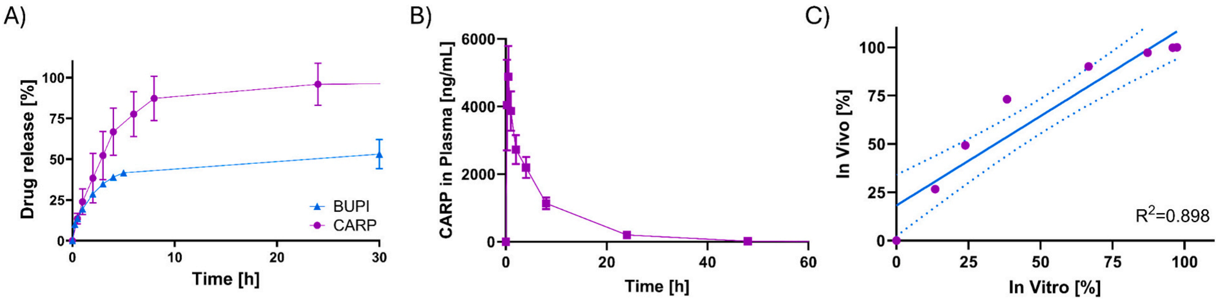

Fig. 3. Comparison of bupivacaine (BUPI) and carprofen (CARP) release from hydrogel and in vivo data. A) Drug release from an agarose-based system, B) pharmacokinetics of subcutaneously administered carprofen in rats, and C) correlation of convoluted in vivo data with in vitro release, shown as a scatter plot with regression line and 90% confidence interval, illustrating the predictive capacity of the in vitro setup.

the qualitative constraints of the s.c. interstitial matrix, consistent with previously reported agarose-based IVIVC systems [58–60]. Accordingly, the IVIVC obtained here should be interpreted as a correlation of cumulative release behavior rather than as a direct predictor of absolute in vivo kinetics; deviations at intermediate time points likely reflect the absence of perfusion and active clearance in the in vitro environment.

Beyond subcutaneous applications, such agarose-based diffusion models may hold promise for other administration routes. For instance, intravitreal drug delivery – currently an area of high interest but limited by the lack of reliable in vitro release systems - could benefit from a similarly straightforward and tunable hydrogel setup [55,66]. Importantly, while this system is easy to implement, laboratory analytics are still required for drug quantification, and cumulative release data cannot be taken as a direct predictor of in vivo behavior [55].

In summary, molded hydrogels provide an accessible and scalable option for early-stage testing, offering a pragmatic balance between simplicity and physiological relevance [58,59]. They also represent a relevant in vitro alternative to animal-derived setups described in the previous sections, thereby further supporting the 3R principles. At the same time, the limitations of release-based data underscore the need for complementary approaches, such as ML models, that can predict pharmacokinetic behavior directly without relying on wet-lab experiments [24,25].

2.4. ML model to predict PK

To further minimize experimental testing and reduce reliance on animal studies, computational modeling offers a powerful complement to laboratory approaches in drug development [6,67,68]. A wide range of models has been explored in PK, particularly for intravenous administration, where mechanistic or physiologically based PK (PBPK) models are often used to capture systemic drug distribution [23–26]. However, such models are typically tailored to very specific scenarios and largely focused on human medicine [23,25]. In contrast, predictive models for veterinary applications remain rare, as research efforts often concentrate on the target species in question [24]. While this organism-specific focus is justified, it leaves a gap in early-stage planning where more generalized models could provide value [13]. By anticipating PK behavior of new compounds, such models can guide experiment design, refine dosing strategies, and reduce variability and animal numbers - aligning well with the 3R principles of replacement, reduction, and refinement [13,24].

Against this background, ML models were developed to predict subcutaneous PK behavior in rodents. With more than 111 million mice and rats used annually in biomedical research in the United States alone, publicly available data from these studies represent a valuable opportunity for training predictive models [69]. A curated dataset based on literature data [70–107] of drugs administered s.c. in rats served as the foundation, from which three separate models were built to predict the key parameters of a one-compartment model: The volume of distribution (V), clearance (Cl), and absorption rate constant (ka) [108]. The choice of V, Cl, and ka, and the use of a one-compartment model, were deliberate. In this framework, these three parameters fully characterize the systemic concentration–time profile following s.c. administration. Clearance Cl determines systemic elimination and, together with V, governs terminal half-life and overall exposure. The volume of distribution V reflects the extent of tissue partitioning versus retention in the central compartment, thereby capturing physicochemical drivers that are particularly relevant to s.c. administration. The constant ka represents uptake from the s.c. depot and integrates processes related to depot dissolution, local diffusion, and vascular or lymphatic transport.

A one-compartment representation was selected to balance simplicity and predictive robustness. Compared with multi-compartment models, this structure reduces the number of target parameters to be estimated while retaining physiologically interpretable quantities that govern exposure. This lower dimensionality is better aligned with the size and heterogeneity of the curated dataset and helps to mitigate overfitting risk, while still capturing the dominant features of systemic disposition following s.c. dosing. In this sense, the model is intended as an early-stage, animal-sparing decision support tool rather than a full mechanistic substitute for in vivo PK evaluation.

The choice of a one-compartment model was deliberate - while not capturing the full complexity of drug distribution, it provides a tractable and sufficiently descriptive framework for small datasets, striking a balance between interpretability, explainability and predictive power [3,108]. While many ML frameworks leverage large data sets colleagues and our lab have shown great model performance even with smaller self-curated data sets [67,109].

Molecular descriptors and dose were used as input features, calculated directly from the molecules' SMILES codes. Gradient boosting regression (XGB) was chosen as the modeling architecture, given its advantages in handling structured datasets of limited size, its robustness against overfitting, and its ability to rank feature importance in an interpretable manner [67]. These properties made XGB particularly suitable for this project, where both predictive accuracy and mechanistic insights into feature contributions were desired [67].

The models were trained and evaluated using a 10-fold cross-validation workflow (Fig. 4A). Here, the dataset was partitioned into ten folds, with iterative training on nine folds and testing on the remaining fold to ensure robust assessment of predictive performance across the entire dataset [110]. To test the generalizability of the model beyond cross-validation, carprofen - a compound not included in the training set - was selected as an external test case. Remarkably, the predicted PK curve closely matched the experimentally determined in vivo profile (Fig. 4B), with a root mean squared error (RMSE) of 0.81. Given the inherent biological variability in PK data and the small training dataset, this level of agreement represents a strong predictive performance [111]. It demonstrates that the model is not only capable of interpolating within known chemical space but also extrapolating to novel compounds with reasonable accuracy [111].

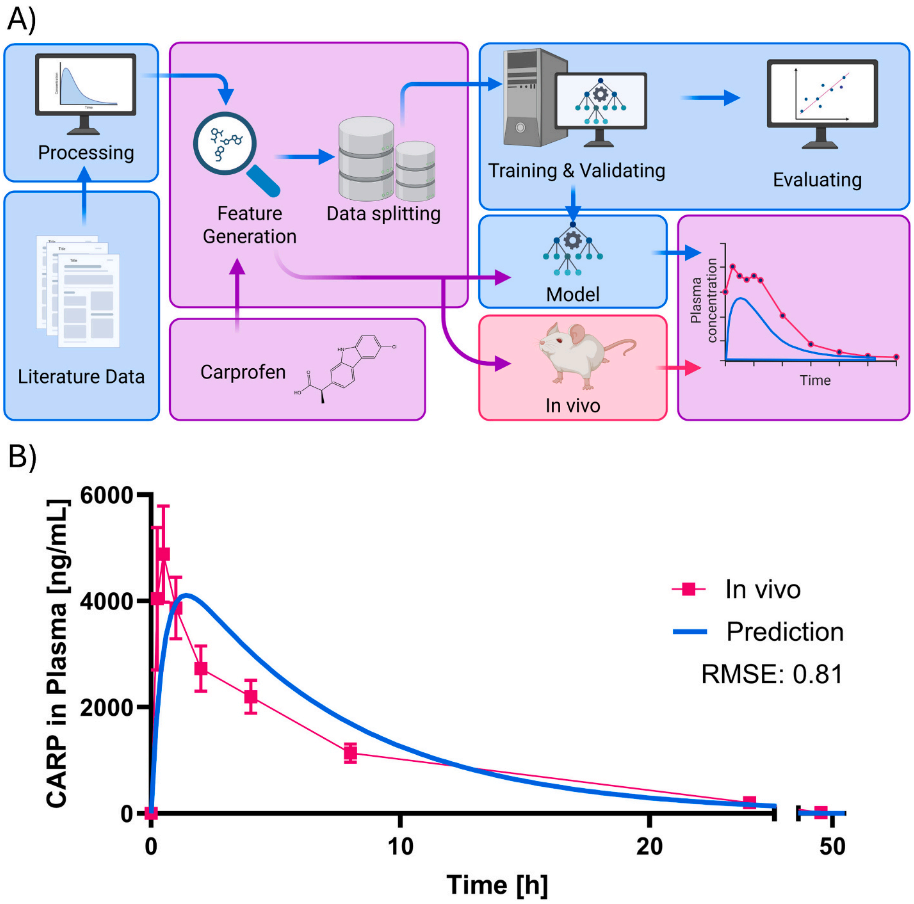

Fig. 4. ML workflow and in vivo validation. A) Workflow of the model: literature data were collected, labels harmonized, and SMILES-based chemical descriptors generated. The dataset was split for training and testing, and model performance was further analyzed using SHAP. Carprofen was used as a case compound, with predicted pharmacokinetic (PK) parameters compared against in vivo data. B) Comparison of predicted PK profile with experimental in vivo PK following subcutaneous administration of carprofen in rats.

The selection of XGBoost was informed by exploratory benchmarking against alternative regression approaches [67]. While linear models showed limited capacity to capture non-linear relationships between physicochemical descriptors and PK parameters, tree-based ensemble methods improved predictive performance but displayed higher variance for small subsets of the data. XGBoost provided the most consistent compromise, with lower cross-validated error dispersion and better handling of moderate feature collinearity. In line with the intended scope of the model, the focus was therefore placed on stability and physiological plausibility of the predictions rather than on maximizing nominal accuracy.

Nevertheless, predictive performance alone does not fully capture the value of an ML model in drug development. Understanding *why* the model makes certain predictions is equally important - both to identify potential sources of bias and to generate mechanistic hypotheses that can be tested experimentally [112,113]. In this context, interpretability methods such as Shapley additive explanations (SHAP) provide valuable insights by quantifying the contribution of each input feature to the model's output [111,113]. Such analyses reveal not only which molecular descriptors are most influential for predicting V, Cl, or ka but also whether their effects are consistent with pharmacological intuition. This interpretability step bridges predictive modeling with experimental science, ensuring that the computational framework remains transparent, trustworthy, and ultimately useful for guiding real-world decisions.

To assess model performance, the coefficient of determination (R^2) was calculated on the basis of the cross-validation to quantify predictive accuracy, yielding values between 0.53 and 0.87. This indicates that 53–87% of the variance in PK parameters was explained by the model, reflecting reliable performance for predictive modeling tasks. Scatter plots of predicted versus experimental values with regression lines (Figs. 5A–C) further illustrate the model's capability. Most datapoints clustered around the regression line, confirming good agreement, though deviations and outliers were observed, particularly at higher V and Cl values. Notably, the model showed a tendency to overestimate V, as reflected by a regression slope below unity. In contrast, predictions for Cl and ka more closely matched the experimental data with slopes approaching 1.

Further, a chemical descriptor and structural distribution analyses (Supporting information) indicate that the dataset covers a representative region of drug-like small-molecule space, while still exhibiting clustered regions and limited coverage of certain chemotypes. As such, residual overfitting risk cannot be fully excluded, even under cross-validation, and the model is therefore interpreted as an early-stage, animal-sparing decision-support tool rather than as a substitute for full PK characterization.

This evaluation highlights both the strengths and the limitations of the model, underscoring its robustness while identifying areas for future refinement.

Tree-based models can capture complex decision-making, but their direct interpretation is often impractical due to depth and rule complexity [67,114]. To address this, feature contributions in the 7-feature XGB model were analyzed using SHAP, an explainable AI (XAI) method well suited for gradient boosting frameworks [67,111,113]. SHAP provides a visual and quantitative interpretation of feature importance and their effect on predictions. Beeswarm plots

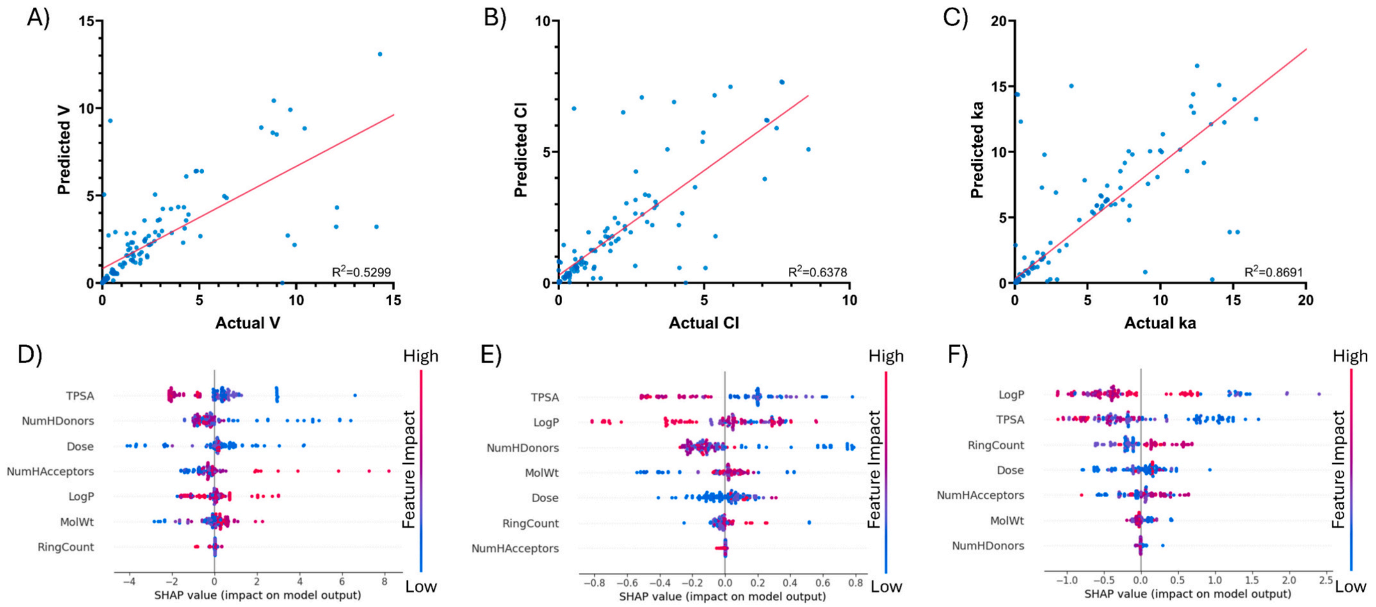

Fig. 5. Model performance and feature impact across prediction targets. A–C) Relationship between experimental and predicted values for volume of distribution (V), clearance (Cl), and absorption rate constant (ka). Coefficients of determination (R^2) from 10-fold cross-validation quantify model performance. D—F) SHAP analysis of the seven-feature XGB regression model, illustrating the impact of individual features on predictions of D) V, E) Cl, and F) ka. Swarm plots show SHAP values, with dot color indicating feature value (magenta for high, blue for low) while horizontal position reflecting positive or negative contributions to the prediction. (For interpretation of the references to color in this figure legend, the reader is referred to the web version of this article.)

(Fig. 5D–F) summarize the impact of each input descriptor on predicted PK parameters, with datapoints representing individual compounds, SHAP values on the x-axis (feature impact), and color indicating feature magnitude. Features are ranked from top to bottom by overall influence, allowing the identification of consistent trends, such as low topological polar surface area (TPSA) contributing positively to V or high LogP exerting a negative effect on ka. These results highlight potential key drivers of PK behavior, including TPSA, hydrogen bonding capacity, LogP, and dose. It should be noted, however, that SHAP evaluates features individually and does not directly account for interactions or synergies among descriptors.

The SHAP analysis yielded mechanistic insights into how molecular descriptors influence pharmacokinetic parameters predicted by the ML models. For the volume of distribution (V), low TPSA and very low H-bond donor counts contributed positively, while higher numbers of H-bond acceptors reduced V. These patterns align with pharmacological principles: reduced polarity favors membrane permeability and tissue partitioning, whereas greater polarity promotes plasma retention [61,115]. Dose showed little overall effect, consistent with mostly non-saturating conditions, though variability at very low doses suggested potential nonlinearities such as protein-binding saturation [115]. Clearance Cl was also strongly shaped by polarity, with low TPSA associated with increased Cl. While this may appear counterintuitive, it likely reflects enhanced hepatic uptake and metabolism of low-TPSA compounds, whereas low LogP favored renal elimination of hydrophilic drugs [116–118]. Very low hydrogen bond donors (HBDs) modestly increased clearance, while low molecular weight correlated with reduced clearance, possibly due to weaker recognition by renal transporters or metabolic enzymes [116–118]. Together, these findings suggest Cl is governed by the balance between polarity, lipophilicity, and molecular size. For absorption rate (ka), lipophilicity dominated: high LogP reduced ka, consistent with solubility-limited depot release in interstitial fluids, while low TPSA enhanced absorption by improving capillary permeability [117,118]. Ring count also played a role, with higher values contributing positively, potentially reflecting rigidity and aromaticity as well as indirectly, lipophilicity, that favor uptake.

Overall, SHAP analysis not only confirmed physiologically plausible relationships but also identified key molecular drivers – TPSA, LogP, hydrogen bonding, and structural features - affecting subcutaneous PK. While descriptor-based models cannot fully capture the mechanistic complexity of clearance and absorption processes, their transparency facilitates hypothesis generation, targeted in vitro follow-up, and refinement of study design, thereby supporting the 3R principles through more informed experiment planning.

A further limitation of the present framework is its focus on free-drug pharmacokinetics. In practice, many therapeutics are administered in formulated delivery systems that can modify depot persistence and release kinetics [7]. Extending the current model to such formulations would require standardized datasets that capture formulation type, carrier–drug interactions, and release behavior, which are presently scarce and highly heterogeneous [119]. Within this constraint, the model is intended to provide a physiologically interpretable baseline estimate of compound-intrinsic systemic disposition in the early phases of development, where drugs are commonly evaluated as free molecules. By enabling prior estimation of key PK parameters and supporting more targeted dose selection and study design, the approach has the potential to reduce exploratory in vivo investigations while preserving scientific rigor [13].

2.5. *Liposomal formulation to treat pain – a case study*

Building on the alternative testing platforms described above, formulation development itself can also serve as a powerful lever to improve animal welfare. In particular, sustained-release strategies reduce both the frequency of dosing and the dependency of patients on caregivers, thereby aligning with the 3R principles [5,8,14,18]. To illustrate how our in vitro models can support such innovations, we used carprofen as clinically relevant case compound and developed a liposomal formulation aimed at to provide prolonged analgesia (48-72 h) following a single subcutaneous injection[110].

A comprehensive formulation study was conducted, in which carprofen was passively loaded into liposomes at different drug-to-lipid ratios (Supporting Information for detailed formulation parameters and optimization data). Physicochemical characterization of a soy-based phospholipid (S80) lead formation (Figs. 6A–C) demonstrated consistently high encapsulation efficiency, nanoscale particle size, and stable zeta potential across all ratios. Here, each dataset corresponds to a specific formulation condition defined by the drug-to-lipid (D/L) ratio and lipid composition; these conditions are displayed as separate groups in the figure legend to facilitate comparison across formulations. At the highest ratio, a slight reduction in zeta potential was observed, likely due to the greater proportion of S80 lipids. Encapsulation efficiency increased with drug-to-lipid ratio, which can be explained by the lipophilicity of carprofen and its affinity for the lipid bilayer [120]. However, maximizing encapsulation is not always the therapeutic goal. As analgesic durg in practice, it may be desirable to leave a fraction of the dose unencapsulated, ensuring a rapid onset of analgesia, followed by sustained release from the encapsulated fraction. Practical considerations also favor moderate drug-to-lipid ratios, as higher lipid contents complicate production, increase formulation viscosity, or require larger injection volumes - all of which may burden patients [121]. Therefore, a 1:30 drug-to-lipid ratio was selected as a favorable option.

Release studies conducted in agarose gels (Fig. 6D) leveraged the system's simplicity and high in vitro–in vivo correlation (IVIVC) as demonstrated in literature before [58,59]. The liposomes displayed biphasic release: an initial burst within the first 8 h, followed by sustained release over several days. Compared to free carprofen release (Fig. 3A), this profile clearly demonstrated the depot function of the liposomes. Importantly, we extended these findings to in vivo PK experiments in rats (Fig. 6E), providing a critical translational link for both the drug formulation and the in vitro system. The in vivo data confirmed a closely matching profile: rapid onset of therapeutic concentrations followed by sustained release for ∼2 days. Such kinetics not only have the potential to provide continuous pain relief but also to reduce both the patient and caregiver burden by extending dosing intervals from every 6–8 h (current standard) to once every 2 days [5,122].

To further evaluate the predictive utility of the agarose release system, in vivo PK data were convoluted to cumulative release and correlated with the in vitro data (Fig. 6F and Supporting Information) [55]. A clear trend was observed ($R^2 = 0.759$), indicating that the agarose model captured more than 75% of the variance in vivo. Nonetheless, systematic deviations were apparent: the system underestimated early release kinetics, likely due to the absence of clearance processes, resulting in an “arched” correlation shape that smoothed out over time. Despite these limitations, the simplicity and low cost of the agarose system make it a valuable tool for early-stage development, particularly for planning experiments with complex depot formulations.

Taken together, this case study highlights how the integration of alternative release models with formulation design can support veterinary applications. By extending analgesic effects and reducing redosing frequency, liposomal systems such as carprofen not only improve animal welfare but also alleviate caregiver workload [122].

3. Conclusion

This study brings together a spectrum of complementary approaches to tackle the complexity of s.c. drug administration while advancing the 3R principles of replacement, reduction, and refinement. By combining ex vivo testing with innovative in vitro models, and complementing these with computational predictions, we provide a toolkit that balances

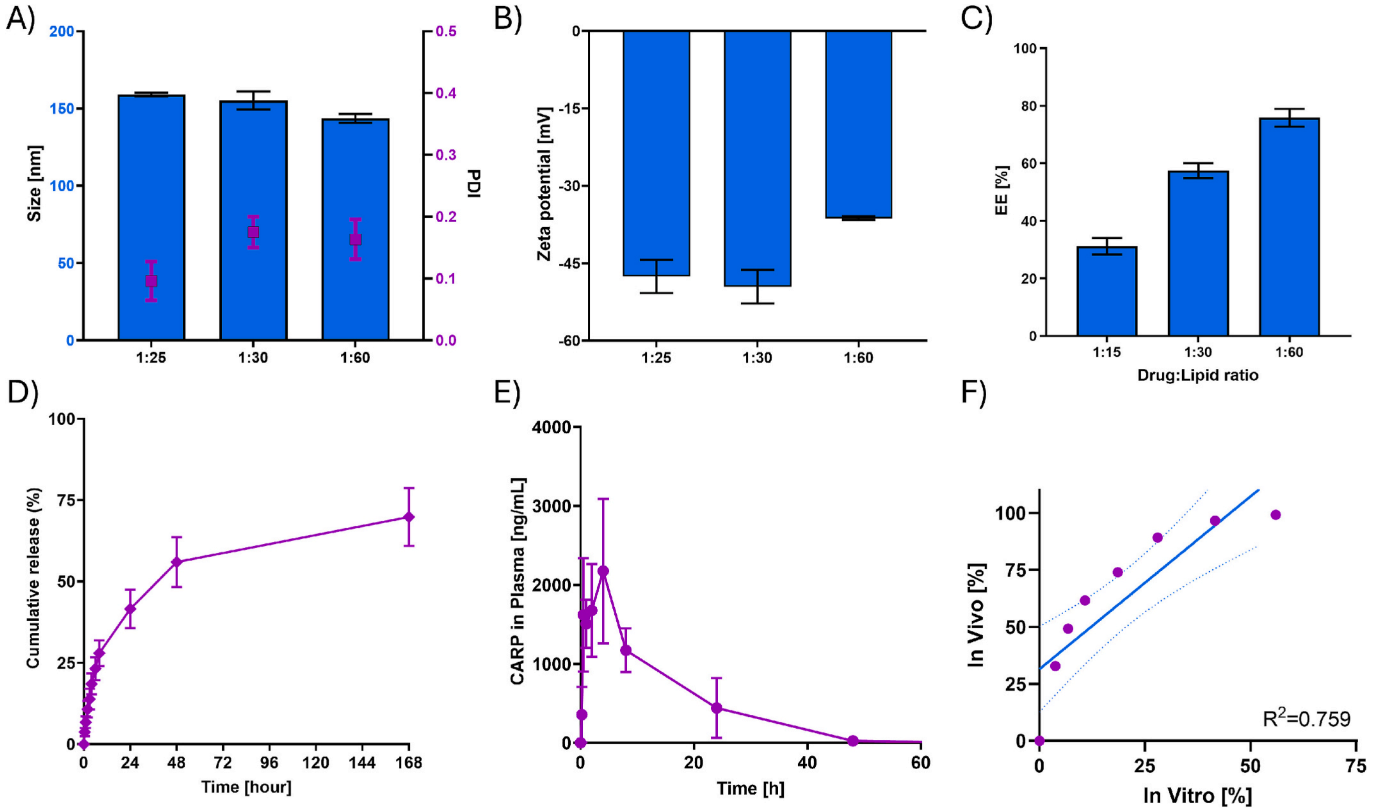

Fig. 6. Liposome characterization and evaluation in vitro and in vivo. A) Hydrodynamic diameter (blue bars, left y axis) and polydispersity index (PDI, purple squares, right y axis) of carprofen-loaded liposomes across different formulation conditions. Individual datasets represent distinct drug-to-lipid ratios and lipid compositions, as indicated in the legend (e.g., D/L 1:25, 1:30; Carprofen:S80). Data are shown as mean ± SD (*n* = 3). B) zeta potential, and C) encapsulation efficiency. D) Carprofen release from liposomes in an agarose-based system, E) pharmacokinetic (PK) profile following subcutaneous administration of carprofen-loaded liposomes in rats, and F) correlation of convoluted in vivo data with in vitro release, shown as a scatter plot with regression line and 90% confidence interval, illustrating the predictive capacity of the in vitro setup. (For interpretation of the references to color in this figure legend, the reader is referred to the web version of this article.)

mechanistic insight with ethical responsibility.

The ex vivo porcine skin model highlighted both the promise and the limitations of traditional tissue-based assays, particularly the variability introduced by tissue sourcing. Building on this, the development of 3D-printed skin constructs and a simple molded agarose hydrogel system demonstrated how more standardized and reproducible release platforms can be achieved. Importantly, the agarose system achieved a strong IVIVC ($R^2 = 0.898$), underscoring its potential as a sustainable and scalable alternative for early-stage screening.

On the computational side, ML models trained on curated datasets were able to predict key PK parameters (V, Cl, ka) with solid accuracy, exemplified by the case of carprofen, where the predicted and observed PK profiles closely aligned (RMSE = 0.81). Beyond accuracy, SHAP analyses revealed physiologically meaningful relationships – such as the strong influence of polarity and lipophilicity on distribution and clearance - demonstrating that these models not only predict but also explain.

Within this framework, the proposed experimental and computational systems are intended to function primarily as upstream screening and prioritization tools, enabling early elimination of unsuitable formulations and more informed hypothesis generation, while subsequent in vivo studies serve as targeted confirmation steps for translational validation.

To support a more transparent comparison of the investigated approaches and to emphasize their complementary rather than substitutive nature, Table 1 provides a concise overview of the main advantages, limitations, and recommended application contexts for each system. This synopsis highlights that no single model fully reproduces the s.c. environment; instead, each method contributes distinct insights that can be strategically combined depending on the scientific question and stage of development.

Finally, the liposomal carprofen case study served as a proof-of-concept scenario, illustrating not only how rational formulation design can extend drug release and reduce dosing frequency, but also how formulation scientists can be supported in their decision-making by the complementary data from in vitro models and ML learning predictions. This integration translates directly into improved animal welfare and caregiver convenience.

Taken together, these results showcase a synergistic framework in which in vitro models, computational tools, and formulation strategies complement one another to reduce animal use without compromising scientific rigor or translational relevance. By highlighting both the opportunities and current limitations, this work points toward a future where predictive, ethical, and mechanistically informed strategies become the standard in s.c. drug development - benefiting not only research but also veterinary and potentially human medicine.

4. Materials and methods

4.1. Materials

Carprofen was obtained from abcr (Germany), while bupivacaine was sourced from Fagron (Germany). A range of lipids including 1,2-dioleoyl-*sn*-glycero-3-phosphocholine (DOPC), 1,2-dioleoyl-*sn*-glycero-3-phospho-(1′-rac-glycerol) (DOPG), soybean phosphatidylcholine (S80), polysorbate 80, 1,2-dipalmitoyl-*sn*-glycero-3-phosphocholine (DPPC), and 1,2-distearoyl-*sn*-glycero-3-phospho-(1′-rac-glycerol) (DSPG) were obtained from Lipoid (Germany). Additional excipients and polymers used in the preparation of model systems included agarose, cholesterol, sodium alginate and hydroxypropyl methylcellulose (HPMC), all purchased from Sigma-Aldrich (Germany).

Analytical reagents such as chloroform, dichloromethane (DCM), methanol, and acetonitrile (ACN) were obtained from Fisher Scientific (Germany), while ethanol was purchased from VWR (Germany). Trifluoroacetic acid (TFA), thienyl, and trypsin were supplied by TCI and Gibco, respectively.

Common laboratory chemicals including HEPES, potassium phosphate, sodium phosphate, Triton X-100, EDTA, Tris, magnesium chloride, sodium azide, and ammonium sulfate were obtained from Carl Roth (Germany). Inorganic salts such as sodium chloride (NaCl) were sourced from Rheinsalinen (Germany), while potassium chloride (KCl) and calcium chloride ($CaCl_2$) were purchased from Sigma-Aldrich. Sodium hydroxide and hydrogen peroxide were provided by Hänseler (Switzerland). Ultrapure water (Milli-Q, MQ) was generated with a Barnstead purification system (Thermo Fisher Scientific).

All chemicals were used as received without further purification, and stock solutions were freshly prepared in Milli-Q water or suitable organic solvents as specified.

5. Methods

5.1. Ex vivo drug release

The ex vivo release for bupivacaine containing drug formulations was assessed using a modified version of an ex vivo dialysis method previously described by Aleandri et al. [18] Briefly, porcine skin was obtained from different sources (Institute of Animal Pathology, University of Bern, Switzerland; Wüthrich Metzg AG, Münchenbuchsee, Switzerland) and cut into skin disks using a circular punch with a diameter of 15 mm. Donor animals older than 110 days were randomly selected. All animals were examined by a veterinarian and deemed healthy based on clinical assessment and macroscopic appearance (no histological evaluation was performed). Skin samples were transported, and stored at 4 °C, and experiments were conducted immediately after harvesting. Commercially available mini dialysis devices with a regenerated cellulose membrane with a molecular weight cut-off of 3.5 kDa by Thermo Fisher Scientific Inc. (Waltham, MA, USA) were used. The lower chamber was filled with 44.5 mL of buffer (Tris 50 mM, NaCl 200 mM, $MgCl_2$ 1.5 mM, $CaCl_2$ 2.5 mM, NaN_3 0.02 *w*/*v*%, pH 7.4) (Tris+), after which the dialysis membrane was inserted. The membrane was wetted with 100 μL of Tris+ and the ex vivo skin disk was placed on top (dermal side facing upwards). Unless otherwise stated, 80 μL of drug-containing formulation (2.5 mg/mL bupivacaine) was injected subcutaneously

Table 1
Comparative assessment of the alternative approaches investigated.

Approach	Key advantages	Main limitations	Most suitable applications
Ex vivo skin model	Preserves native tissue architecture and microstructure; high biological relevance; suitable for mechanistic observations of depot–tissue interaction	High inter-sample variability; dependence on tissue origin and handling; limited reproducibility and ethical dependency on animal-derived material	Early mechanistic assessment of depot formation and diffusion in native tissue
3D-printed artificial tissue	Standardized and reproducible; tunable composition; reduced biological variability compared to native tissue; printable on demand	Requires specialized equipment and labor-intensive preparation; still partly dependent on animal-derived components; lacks active clearance and perfusion	Controlled in vitro comparison of formulations and design-space exploration
Agarose hydrogel system	Simple, low-cost and scalable; highly reproducible; good IVIVC for cumulative release behavior; suitable for routine screening	Lacks biological microstructure and clearance processes; diffusion-dominated environment; not a direct surrogate for in vivo PK	High-throughput screening and formulation ranking at early development stage
ML-based PK prediction	No wet-lab material required; enables prior estimation of PK parameters; supports experimental planning and dose selection; contributes to 3R by reducing exploratory studies	Depends on dataset coverage and quality; currently limited to free drugs and one-compartment PK assumptions	Early decision-making, feasibility assessment, and refinement of in vivo study design

using 27 gauge needles (B. Braun, Melsungen, Germany) into the skin disk, and the dialysis tubes were subsequently placed in an incubator (37 °C, 70 rpm). At specific time points, 1 mL of medium was withdrawn from the lower chamber for analysis and replaced with fresh Tris+ and subsequently quantified.

5.2. In vitro in vivo correlation (IVIVC) analysis

IVIVC was established by directly correlating the drug's in vitro dissolution profile with its in vivo absorption profile.

All data processing and statistical analyses were performed using Python with the pandas, NumPy, scikit-learn, and Matplotlib libraries.

The in vitro dissolution data, provided as cumulative percentage drug released, were collected from three replicates at each specified time point. The mean cumulative percentage drug released was calculated for each time point to represent the average in vitro dissolution profile.

The in vivo absorption profile was derived from the mean plasma concentration-time data using the Wagner-Nelson deconvolution method. This method is suitable for drugs that follow a one-compartment model with first-order elimination after oral administration. The key steps of the deconvolution process were as follows:

1. Calculation of Area Under the Curve (AUC) from Time 0 to t (AUC0 → t): The area under the plasma concentration-time curve up to each time point, t, was calculated using the linear trapezoidal rule. For each time interval, the AUC was calculated using the equation:

$$AUC_t = \frac{(C_{pi-1} + C_{pi})}{2}(t_i - t_{i-1})$$

The cumulative AUC0 → t was then obtained by summing the AUCs of all preceding intervals.

2. Determination of the Terminal Elimination Rate Constant (ke): The elimination rate constant (ke) was determined from the terminal log-linear phase of the plasma concentration-time curve. This was achieved by performing a linear regression analysis on the natural logarithm of the plasma concentrations against time for the time points where the concentration decline was monoexponential. The slope of this regression line corresponds to −ke.
3. Calculation of Total AUC (AUC0 → ∞): The total AUC from time zero to infinity (AUC0 → ∞) was calculated by adding the extrapolated AUC from the last measured time point to infinity to the cumulative AUC up to that point. The extrapolation was based on the terminal elimination rate constant (ke).

$$AUC_{0\to\infty} = AUC_{0\to t_{last}} + \frac{C_{pi\ last}}{k_e}$$

4. Calculation of Cumulative Percentage Absorbed: The cumulative fraction of drug absorbed (Fa) at each time point was calculated using the Wagner-Nelson equation:

The cumulative fraction was then multiplied by 100 to obtain the cumulative percentage drug absorbed at each time point.

$$F_a = \frac{C_{pi} + k_e \bullet AUC_{0\to t}}{k_e \bullet AUC_{0\to\infty}}$$

5.3. IVIVC plot and statistical correlation

A graph was generated by plotting the mean cumulative percentage drug released (in vitro) on the x-axis against the calculated cumulative percentage drug absorbed (in vivo) on the y-axis. A linear regression analysis was performed on this plot to assess the strength of the correlation. The coefficient of determination (R2) was calculated to quantify the goodness of fit of the linear model, providing a metric for the predictive power of the in vitro dissolution data.

5.4. Bioink and 3D printing

For the production of porcine skin powder (PSP), an adjusted method from Wolf et al. was used [45]. Briefly, the dermis was finely chopped and treated with trypsin (0.25%, 6 h) while being shaken at 300 rpm. The tissue was then washed four times with distilled water before adding EtOH (70%, 16 h). After removal of the EtOH, the samples were treated three times using H_2O_2 (3%, 15 min), The tissue is again washed three times with distilled water, with subsequent addition of an aqueous Triton X-100 solution (1% *w/v* Triton X-100, 0.26% w/v EDTA, 0.69% w/v Tris, pH 7.4, 24 h, 300 rpm). The samples are washed three times with distilled water, before being frozen using liquid nitrogen and lyophilized overnight until dry. The dry samples were frozen again and kept at cryogenic temperatures while being crushed in a mortar. The crushed frozen PSP was stored at −25 °C.

An artificial tissue simulate (AT) was prepared, consisting of ALG, PSP, HPMC and buffer (HEPES 50 mM, NaCl 135 mM, KCl 4 mM, $MgCl_2$ 6 H_2O 0.5 mM, $CaCl_2$ 1.6 mM, NaN_3 0.02% w/v, pH 7.4) (HEPES+). ALG was left to dissolve in HEPES+ overnight under continuous stirring, before being mixed with the other components. Additionally, 10% *v*/v of a calcium solution (200 mM) was added for internal stability. The homogenous mixture was loaded into 3 mL pneumatic cartridges (Cellink, Göteborg, Sweden) and printed using Bio X 3D Bioprinter (Cellink, Göteborg, Sweden) using semi-solid extrusion following a cylindrical 3D model ($r = 7.5$ mm, h = 15 mm). The nozzle size and printing speed were kept constant at 22 gauge and 10 mm/s respectively. For cross-linking, the printed cylinders were submerged in a $CaCl_2$ solution (150 mM, 1 h) before being stored at 4 °C.

5.5. Design of Experiments (DoE)

A mixture design of experiment (DoE) was used to investigate the effect of the bioink's composition and printing parameters on the printability of the disks and the injectability of MQ water into the AT disks. For each of the four components an upper and lower limit was determined (Table 2). Further were two process parameters identified, being printing pressure and infill density. A total of 44 runs were conducted in random order. The printability was assessed using a scale from one to five (for the detailed scale: see SI). The injectability was determined after injection of 200 μL of MQ into the middle of the disk using a 27 gauge needle, following a similar scale from one to five (for the detailed scale, Supporting Information). The obtained data were evaluated using Minitab 18 software (Minitab Inc., Pennsylvania, USA). Regression coefficients were determined for the components and the interactions with a confidence interval of 95%. The average distance

Table 2
DoE factors and levels.

Component		
	Lower Limit	Upper Limit
PSP	5 (% *w*/w)	10 (% w/w)
ALG	5 (% w/w)	15 (% w/w)
HPMC	5 (% w/w)	15 (% w/w)
HEPES +	50 (% w/w)	75 (% w/w)
Ca^{2+} solution	20 (mM)	
Process variable		
	Lower Limit	Upper Limit
Printing pressure	60 (kPa)	90 (kPa)
Infill density	20 (%)	50 (%)

from observed values to the regression line (S), R^2, and adjusted R^2 were used to assess the model's accuracy. A final composition was determined using Minitab to optimize both printability and injectability.

5.6. *Drug release from artificial tissue*

The in vitro release for both drugs was assessed using a modified version of an ex vivo dialysis method previously described by Aleandri et al. [18] Briefly, commercially available mini dialysis devices with a regenerated cellulose membrane with a molecular weight cut-off of 3.5 kDa by Thermo Fisher Scientific Inc. (Waltham, MA, USA) were used. The lower chamber was filled with 44.5 mL of buffer (Tris 50 mM, NaCl 200 mM, $MgCl_2$ 1.5 mM, $CaCl_2$ 2.5 mM, NaN_3 0.02 *w/v*%, pH 7.4) (Tris+), after which the dialysis membrane was inserted. The membrane was wetted with 100 μL of Tris+ and the 3D-printed AT was placed on top. Unless otherwise stated, 80 μL of drug-containing formulation (2.5 mg/mL bupivacaine) were injected manually using 27 gauge needles (B. Braun, Melsungen, Germany) centrally at a 45° angle into the AT disk and the dialysis tubes were subsequently placed in an incubator (37 °C, 70 rpm). At specific time points, 1 mL of medium was taken from the lower chamber and replaced with fresh Tris+ and subsequently quantified.

5.7. *Drug release from agarose system*

The in vitro release of carprofen was first assessed using a slightly modified version of the agarose release setup first described by Bassand et al. [60] Briefly, a suspension of agarose (1.0% *w/v*) in HBS was heated to 100 °C in a microwave. The suspension was then stirred (250 rpm) at 47 °C until a clear solution was achieved. A diluted solution (0.5% w/v agarose) was derived from it. To prevent gelation, both solutions were kept at 47 °C and stirred continuously. Into a 5 mL Eppendorf tube, 900 μL of the 0.5% w/v agarose solution were added, after which a cylindrical, flat-ended metallic rod was suspended 3.6 cm into the still hot solution without touching the walls of the tube (Fig. S6 & S7). After 3 min at room temperature, the metal rod was removed, creating an empty pocket within the agarose gel. Into the pocket, 100 μL of liposomal dispersion were added before additional 100 μL of 1% w/v agarose solution were layered on top of it. To facilitate gelation, the tube was kept 5 min at room temperature.

Next, 400 μL of 0.5%w/v agarose solution were layered on top and gelification was allowed to occur for 5 min at room temperature.

To start the release, 1 mL of HBS was added on top of the agarose gel and the closed tube placed in an incubator (37 °C, 100 rpm). At predetermined time points (1/2, 1, 2, 3, 4, 6, 8, 24, 48 and 168 h), the entire volume was withdrawn and completely replaced by fresh (pre-heated) release medium. Of this withdrawn volume, 500 μL were lyophilized and subsequently resuspended in MeOH (250 μL), vortexed (10 min), sonicated (10 min, 45 °C), and finally centrifuged (24′000 ×*g*, 10 min). From each sample, 100 μL of the supernatant was analyzed as described above.

5.8. *In vivo studies*

All animal experiments were performed on 12-week-old Lewis rats (BW: F185g / M330g) (LEW/OrlRj, Janvier Laboratories, France) in accordance with institutional and federal regulations governing animal care and use, the PREPARE and ARRIVE guidelines, and were approved by the Cantonal Veterinary Office of Bern (Switzerland) (BE47/2021). Rats were housed in specific pathogen-free (SPF) facility. The housing conditions were controlled with a 12:12 h light: dark cycle, room temperature in the range of 22±2 °C and relative humidity in the range of 45%–65%. Autoclaved tap water and irradiated rodent chow (Mouse and Rat Maintenance 3432, Granovit, Switzerland) were provided ad libitum. Up to 3 rats were be accommodated in autoclaved IVCs cages (1500 cm^2 Blue line, Tecniplast, Italy) with aspen wood bedding (J. Rettenmeier & Söhne GmbH, Germany) and enrichments. The rats underwent a one-week acclimatization period and were regularly handled by personnel to gently habituate them to the procedures. On the day of experiment, animals were randomly allocated to different treatment groups, and treatments were blinded for the researchers. Each group, consisting of equivalent males and females, received a different treatment, and the sex was then imposed as a blocking factor for the statistical analysis. The results are presented as mean ± σ or mean ± SEM. For the pharmacokinetics study, the rats ($n = 4$/group, sex balanced) received 0.8 mg/kg free drug (Carprofen) or carprofen encapsulated into the liposomal system via subcutaneous injection (n = 4/group, sex-balanced) at the base of the neck. Blood samples (100 μL) were collected from the lateral tail vein at the following time points: −2 days (baseline), 0.25, 0.5, 1, 2, 4 and 8 h, and 1, 2, 3, 4, 7, 9, 11, and 14 days post-injection. Sampling was performed with conscious animals placed in a restrainer. Animals were euthanized by CO_2 inhalation after the final sampling point. Collected blood was transferred into K_2-EDTA BD Microtainer™ tubes (Fisher Scientific AG, Switzerland), centrifuged at 4 °C for 5 min at 3′000 g, and the resulting plasma (25 μL) was stored at −20 °C until analysis. For drug quantification, carprofen was extracted from plasma by adding 125 μL of methanol containing deuterated carprofen as an internal standard and 100 μL of acetonitrile. Samples were centrifuged at 20′000 *g* for 1 h at 4 °C, and the drug concentration in the resulting supernatant was measured using LC-MS/MS on a Sciex QTrap 5500 instrument (AB Sciex Switzerland GmbH) equipped with an UltiMate 3000 HPLC system (Thermo Fisher Scientific, Switzerland). Quantitation of CARP was performed by multiple reaction monitoring.

5.9. *Liposome preparation*

Liposomes were prepared according to the thin-film hydration method, followed by extrusion and freeze-thaw cycles [121]. Due to differences in the hydrophobicity of the used drugs, different protocols were used for the encapsulation within the liposomes. The hydrophobic carprofen was encapsulated passively. For this, carprofen dissolved in MeOH was transferred into an amber glass vial, to obtain a final carprofen concentration of 0.1 mg/mL. Into the same vial, appropriate amounts of lipid stock solutions in chloroform were added to achieve the selected drug-to-lipid ratios and final lipid compositions. Under an inert gas stream, the organic solvent was removed, after which the films where further dried under vacuum. To hydrate proper amounts of 25 mM HEPES, 140 mM NaCl aqueous buffer (pH 7.4) (HBS) were added forming multilamellar vesicles (MLVs). The suspension was extruded 10 times through a 200 nm polycarbonate membrane (Sterlitech, USA) using a LIPEX® extruder (Evonik, Canada) kept at 65 °C and MLVs loaded with carprofen (CARP-MLV) were obtained. To prepare small unilamellar vesicles (SUVs), the hydrated MLV suspension was frozen with liquid nitrogen (2 min) and thawed in a water bath at 65 °C (6 min) six times before extrusion (CARP-SUV). For scale up studies, carprofen concentration was increased to 2 mg/mL while the lipid concentration was adjusted.

The hydrophilic bupivacaine was encapsulated using a transmembrane pH gradient. [18,121] First, appropriate amounts of stock solutions of DPPC, DSPG, and cholesterol in chloroform were added into glass vials to achieve mol percentages of 45:25:30. The organic solvent was evaporated using a nitrogen gas stream before drying under vacuum overnight. The films were hydrated using $(NH_4)_2SO_4$ (150 mM) solution, before being subjected to 6 freeze-thaw-cycles in liquid nitrogen (2 min) and a water bath at 70 °C (6 min), and extruded 10 times through a 200 nm polycarbonate membrane using a LIPEX® extruder kept at 70 °C. For the transmembrane gradient the external buffer was replaced by NaCl (150 mM) solution. For this Sephadex G50 columns (swollen in 150 mM NaCl solution) were loaded with the liposome suspension. The eluted liposomes were collected before being mixed with appropriate amounts of an aqueous bupivacaine stock solution to achieve a drug-to-lipid ratio of 1:1 and incubated at 70 °C for 30 min. Using the same columns a size exclusion chromatography (SEC) was performed to remove unencapsulated bupivacaine. The bupivacaine loaded liposomes (BUPI-SUV) were concentrated by centrifugation using Amicon® Ultra-15 (regenerated cellulose, RC, Cut-off 10′000 MW; Merck Millipore, Massachusetts, USA).

5.10. *In Silico modeling*

A supervised machine learning workflow was developed to predict the pharmacokinetic parameters governing the systemic exposure of subcutaneously administered small molecules. The dataset was curated from the literature as described above and comprised 124 compound–dose PK records. For each entry, physicochemical descriptors (molecular weight, LogP, topological polar surface area, hydrogen-bond donors/acceptors, rotatable bonds or ring count) together with the administered dose were used as input features, while the PK targets were the volume of distribution (V), clearance (Cl), and absorption rate constant (ka). Feature scaling was applied using a fitted standardization transform to ensure consistency between training and prediction.

The three target parameters were selected because they fully define the systemic concentration–time profile within a one-compartment model with first-order absorption. The corresponding one-compartmental analytical solution was used for PK reconstruction and visualization:

$$C(t) = \frac{F \cdot D \cdot k_a}{V(k_a - k_e)}\left(e^{-k_e t} - e^{-k_a t}\right) \text{ with } k_e = \frac{Cl}{V}.$$

where F is bioavailability, $D$the administered dose, $k_a$the absorption rate constant, k_e the elimination rate constant, V the volume of distribution, and Cl the clearance. During preliminary benchmarking, several regression algorithms (decision tree, random forest, and gradient-boosting variants) were evaluated. XGBoost was ultimately selected because it provided the most favorable bias–variance trade-off under 10-fold cross-validation and yielded stable predictions across all three PK targets.

To characterize dataset diversity, an exploratory chemical-space analysis was performed based on molecular weight, LogP, topological polar surface area (TPSA), hydrogen-bond donor and acceptor counts, and number of rotatable bonds. Further, t-distributed stochastic neighbor embedding, using Morgan fingerprints was used to map the data set in chemical space. The corresponding distributions are reported in Supporting Information.

5.11. *Dynamic light scattering (DLS)*

The mean hydrodynamic diameter, the polydispersity index (PDI) and the zeta potential of liposomes were measured using a Litesizer500® (Anton Paar; Graz, Austria) with a 173° backscatter angle and a 658 nm helium–neon-laser. For size measurements, 10 μL of sample was diluted in 990 μL buffer. After equilibrating at 25 °C, the measurement (at least 15 runs×10 s) was performed. As the intensity size distribution of the liposomes was typically unimodal, the autocorrelation function was analyzed according to the cumulant method by the Kalliope™-software. [123] For zeta potential measurements, 10 μL of sample were diluted in 990 μL of MilliQ. The instrument was set at 200 V and 30 runs for CARP-MLV and CARP-SUV and 100 runs for BUPI-SUV were performed. The Smoluchowski approximation with a Debye factor of 1.5 was used to calculate the mean zeta potential value.

5.12. *Drug loading and encapsulation efficiency*

Purification was performed using PD Mini-Trap Sephadex G-25 resin desalting column. A volume of 0.5 mL freshly prepared liposomes was loaded into the column and eluted using HBS. Fractions (20 × 0.5 mL) were collected and analyzed using dynamic light scattering. The absolute intensity in kilocounts per second (kcps) was plotted against the elution volume. Similarly, the elution profile of free carprofen was recorded by adding a saturated carprofen solution to the same column, eluting with HBS and quantifying the carprofen content in 30 fractions. The carprofen content was plotted against the elution volume. From this the liposome containing fractions can be identified (Supporting information).

Carprofen quantification was carried out using an Infinite M Pro 200F-PlexNano microplate reader (Tecan; Männedorf, Switzerland). A carprofen calibration curve was prepared in MeOH (0.49 μg/mL - 62.75 μg/mL) and absorbance was measured at 302 nm using a quartz microplate (Hellma analytics; Müllheim, Germany). The carprofen concentration was plotted against absorbance, and a regression equation was computed ($Y = 0.01419{*}X + 0.003895$, $R^2 = 0.9998$, $n = 3$). To assure quality and accuracy of the method independent samples of carprofen in MeOH solution were measured and back calculated.

Bupivacaine quantification was carried out using an Ultimate 3000RS high pressure liquid chromatography (HPLC) system by Dionex Softron (Germering, Germany) equipped with a LPG-3400SD pump, a WPS-3000TFC analytical autosampler, a TCC-3000RS thermostat column compartment, a DAD-3000RS diode array detector. and a NUCLEOSIL 100–5 C18 column by Macherey-Nagel (Oensingen, Switzerland). Using lidocaine as an internal standard (IS), peak area ratios of BUPI/IS were measured over a range BUPI concentrations (1.56 μg/mL – 100 μg/mL) and plotted against the BUPI concentration. A linear regression was calculated ($Y = 0.001895{*}X + 0.0004511$, $R^2 = 0.9952$, $n = 3$) and used for further quantification. Samples were lyophilized and resuspended in MeOH (250 μL) containing 0.5 mg/mL IS before injection (for details on the method: see SI).

5.13. *Statistics and reproducibility*

All statistical analyses performed are available for each experiment in the results & discussion section of the manuscript. No data were excluded from the analysis. GraphPad Prism 10.2.3 (GraphPad Software, USA) and R 4.4.0 (The R Foundation, Germany) were used for statistical analysis.

CRediT authorship contribution statement

Remo Eugster: Writing – original draft, Visualization, Validation, Methodology, Investigation, Formal analysis, Data curation, Conceptualization. **Niklaas Manten:** Writing – review & editing, Visualization, Validation, Methodology, Investigation, Formal analysis. **Giorgio Buttitta:** Writing – review & editing, Validation, Methodology, Investigation, Formal analysis. **Götz Chwatal:** Writing – review & editing, Validation, Methodology, Investigation. **Stefan Schürch:** Writing – review & editing, Methodology, Investigation. **Alessandra Bergadano:** Writing – review & editing, Methodology, Conceptualization. **Simone Aleandri:** Writing – review & editing, Supervision, Methodology, Investigation, Data curation, Conceptualization. **Paola Luciani:** Writing – review & editing, Supervision, Resources, Funding acquisition, Conceptualization.

Code availability

The source codes that support the findings of this study are publicly available on GitHub (https://github.com/Luciani-Group/Code) was written and executed in Python 3.11.9 in an Anaconda 24.3.0 environment. Python packages and libraries used are disclosed on GitHub.

Declaration of competing interest

No private study sponsors had any involvement in the study design, data collection, or interpretation of data presented in this manuscript. P. L. declares the following competing interests: she has consulted and received research grants from Lipoid GmbH, Sanofi-Aventis Deutschland and DSM Nutritional Products Ltd.; she received research grants from PPM Services S.A.

Acknowledgement

We would like to thank Kevin Weber-Wilk and Maria Nanni for their support during PK studies. Also, we would like to thank Claudia Bühr for technical assistance with LC/MS analytics. We respectfully acknowledge the animals involved in this research, with the goal of advancing approaches that minimize the need for animal experimentation in the future.

Appendix A. Supplementary data

Supplementary data to this article can be found online at https://doi.org/10.1016/j.jconrel.2026.114863.

Data availability

All data generated or analyzed during this study are included in this published article and its supplementary information file. The complete datasets used for training and testing the machine learning models are publicly available as .csv files on GitHub (https://github.com/Luciani-Group/).

The complete datasets used for training and testing the machine learning models are publicly available as .csv files on GitHub (https://github.com/Luciani-Group/Sc_Pharmacokinetics).

References

[1] Tomasini Lorenzo, Ferrere Marianne, Nicolas Julien, Subcutaneous drug delivery from nanoscale systems, Nat Rev Bioeng 2 (2024) 501–520, https://doi.org/10.1038/s44222-024-00161-w.

[2] I.R. Dubbelboer, E. Sjögren, Overview of authorized drug products for subcutaneous administration: pharmaceutical, therapeutic, and physicochemical properties, Eur. J. Pharm. Sci. 173 (2022) 106181, https://doi.org/10.1016/j.ejps.2022.106181.

[3] L. Kagan, Pharmacokinetic modeling of the subcutaneous absorption of therapeutic proteins, Drug Metab. Dispos. 42 (2014) 1890–1905, https://doi.org/10.1124/dmd.114.059121.

[4] H.M. Kinnunen, R.J. Mrsny, Improving the outcomes of biopharmaceutical delivery via the subcutaneous route by understanding the chemical, physical and physiological properties of the subcutaneous injection site, J. Control. Release 182 (2014) 22–32, https://doi.org/10.1016/j.jconrel.2014.03.011.

[5] C.M. Manasa, U. Likhitha, U.Y. Nayak, Revolutionizing animal health: A comprehensive review of long-acting formulations, J. Drug Delivery Sci. Technol. 101 (2024) 106226, https://doi.org/10.1016/j.jddst.2024.106226.

[6] R. Eugster, S. Aleandri, J. Bassila, D. Bochicchio, L. Baraldi, B. Hämmerle, S. Schürch, M. Vermathen, P. Vermathen, G. Rossi, A. Bergadano, P. Luciani, Physiologically controlled release from an in situ forming liposomal depot, J. Control Release 392 (2026) 114739, https://doi.org/10.1016/j.jconrel.2026.114739.

[7] Wei Li, Jie Tang, Dennis Lee, Thomas R. Tice, Steven P. Schwendeman, Mark R. Prausnitz, Clinical translation of long-acting drug delivery formulations, Nat. Rev. Mater. 7 (2022) 406–420, https://doi.org/10.1038/s41578-021-00405-w.

[8] V. Schreiner, M. Durst, M. Arras, P. Detampel, P. Jirkof, J. Huwyler, Design and in vivo evaluation of a microparticulate depot formulation of buprenorphine for veterinary use, Sci. Rep. 10 (2020) 17295, https://doi.org/10.1038/s41598-020-74230-6.

[9] T. McDonald, M. L Zepeda, M. Tomlinson, W. Bee, I. Ivens, Subcutaneous administration of biotherapeutics: Current experience in animal models, Curr. Opin. Mol. Ther. 12 (927) 461–470.

[10] J. Østergaard, N. Mertz, V. Gancho, A. Le, M. Barber, P. Bezawada, S.W. Larsen, M.N. O`Brien Laramy, J. Rohit, Development of a bio-relevant in vitro release testing method for subcutaneous and intramuscular oil depot formulations, J. Drug Delivery Sci. Technol. 102 (2024) 106412, https://doi.org/10.1016/j.jddst.2024.106412.

[11] A. Akhtar, The flaws and human harms of animal experimentation, Camb. Q. Healthc. Ethics 24 (2015) 407–419, https://doi.org/10.1017/S0963180115000079.

[12] S.H. Richter, Challenging current scientific practice: how a shift in research methodology could reduce animal use, Lab. Anim. 53 (2024) 9–12, https://doi.org/10.1038/s41684-023-01308-9.

[13] P. Rinwa, M. Eriksson, I. Cotgreave, M. Bäckberg, 3R-refinement principles: elevating rodent well-being and research quality, Lab Anim Res 40 (2024) 11, https://doi.org/10.1186/s42826-024-00198-3.

[14] A. Wolter, C.H. Bucher, S. Kurmies, V. Schreiner, F. Konietschke, K. Hohlbaum, R. Klopfleisch, M. Löhning, C. Thöne-Reineke, F. Buttgereit, J. Huwyler, P. Jirkof, A.E. Rapp, A. Lang, A buprenorphine depot formulation provides effective sustained post-surgical analgesia for 72 h in mouse femoral fracture models, Sci. Rep. 13 (2023) 3824, https://doi.org/10.1038/s41598-023-30641-9.

[15] L. Rahnfeld, P. Luciani, Injectable lipid-based depot formulations: where do we stand? Pharmaceutics 12 (2020) 1–28, https://doi.org/10.3390/pharmaceutics12060567.

[16] G. Ouedraogo, N. Alépée, B. Tan, C.S. Roper, A call to action: advancing new approach methodologies (NAMs) in regulatory toxicology through a unified framework for validation and acceptance, Regul. Toxicol. Pharmacol. 162 (2025) 105904, https://doi.org/10.1016/j.yrtph.2025.105904.

[17] C. Harrison, FDA pushes to replace animal testing, Nat. Biotechnol. 43 (2025) 655–656, https://doi.org/10.1038/s41587-025-02690-0.

[18] S. Aleandri, L. Rahnfeld, D. Chatzikleanthous, A. Bergadano, C. Bühr, C. Detotto, S. Fuochi, K. Weber-Wilk, S. Schürch, P. van Hoogevest, P. Luciani, Development and in vivo validation of phospholipid-based depots for the sustained release of bupivacaine, Eur. J. Pharm. Biopharm. 181 (2022) 300–309, https://doi.org/10.1016/j.ejpb.2022.11.019.

[19] S. Runser, R. Vetter, D. Iber, SimuCell3D: three-dimensional simulation of tissue mechanics with cell polarization, Nat Comput Sci 4 (2024) 299–309, https://doi.org/10.1038/s43588-024-00620-9.

[20] C. Bender, S. Eichling, L. Franzen, V. Herzog, L.M. Ickenstein, D. Jere, L. Nonis, G. Schwach, P. Stoll, M. Venczel, S. Zenk, Evaluation of in vitro tools to predict the in vivo absorption of biopharmaceuticals following subcutaneous administration, J. Pharm. Sci. 111 (2022) 2514–2524, https://doi.org/10.1016/j.xphs.2022.04.005.

[21] I. Torres-Terán, M. Venczel, S. Klein, Prediction of subcutaneous drug absorption – development of novel simulated interstitial fluid media for predictive subcutaneous in vitro assays, Int. J. Pharm. 658 (2024) 124227, https://doi.org/10.1016/j.ijpharm.2024.124227.

[22] R. Satheeskumar, Enhancing drug discovery with AI: predictive modeling of pharmacokinetics using graph neural networks and ensemble learning, Intelligent Pharmacy 3 (2025) 127–140, https://doi.org/10.1016/j.ipha.2024.11.002.

[23] Z. Huang, P. Denti, H. Mistry, F. Kloprogge, Machine learning and artificial intelligence in PK-PD Modeling: fad, friend, or foe? Clin. Pharmacol. Ther. 115 (2024) 652–654, https://doi.org/10.1002/cpt.3165.

[24] O. Obrezanova, A. Martinsson, T. Whitehead, S. Mahmoud, A. Bender, F. Miljković, P. Grabowski, B. Irwin, I. Oprisiu, G. Conduit, M. Segall, G.F. Smith, B. Williamson, S. Winiwarter, N. Greene, Prediction of in vivo pharmacokinetic parameters and time-exposure curves in rats using machine learning from the chemical structure, Mol. Pharm. 19 (2022) 1488–1504, https://doi.org/10.1021/acs.molpharmaceut.2c00027.

[25] X. Jia, D. Teutonico, S. Dhakal, Y.M. Psarellis, A. Abos, H. Zhu, P.D. Mavroudis, N. Pillai, Application of machine learning and mechanistic Modeling to predict intravenous pharmacokinetic profiles in humans, J. Med. Chem. 68 (2025) 7737–7750, https://doi.org/10.1021/acs.jmedchem.5c00340.

[26] O. Obrezanova, Artificial intelligence for compound pharmacokinetics prediction, Curr. Opin. Struct. Biol. 79 (2023) 102546, https://doi.org/10.1016/j.sbi.2023.102546.

[27] S. Gou, Y.N. Kalia, Development of an ex vivo human skin model and evaluation of biological responses to subcutaneously injected hyaluronic acid formulations, Int. J. Pharm. 674 (2025) 125490, https://doi.org/10.1016/j.ijpharm.2025.125490.

[28] Y. Xu, N. Shrestha, V. Préat, A. Beloqui, An overview of in vitro, ex vivo and in vivo models for studying the transport of drugs across intestinal barriers, Adv. Drug Deliv. Rev. 175 (2021) 113795, https://doi.org/10.1016/j.addr.2021.05.005.

[29] A.A. Merleev, S.T. Le, C. Alexanian, A. Toussi, Y. Xie, A.I. Marusina, S.M. Watkins, F. Patel, A.C. Billi, J. Wiedemann, Y. Izumiya, A. Kumar, R. Uppala, J. Michelle Kahlenberg, F.T. Liu, I.E. Adamopoulos, E.A. Wang, C. Ma, M.Y. Cheng, H. Xiong, A. Kirane, G. Luxardi, B. Andersen, L.C. Tsoi, C.B. Lebrilla, J.E. Gudjonsson, E. Maverakis, Biogeographic and disease-specific alterations in epidermal lipid composition and single-cell analysis of acral keratinocytes, JCI Insight 7 (2022) e159762, https://doi.org/10.1172/jci.insight.159762.

[30] A. Wurbs, C. Karner, D. Vejzovic, G. Singer, M. Pichler, B. Liegl-Atzwanger, B. Rinner, A human ex vivo skin model breaking boundaries, Sci. Rep. 14 (2024) 24054, https://doi.org/10.1038/s41598-024-75291-7.

[31] M.N. Martinez, Factors influencing the use and interpretation of animal models in the development of parenteral drug delivery systems, AAPS Journal 13 (2011) 632–649, https://doi.org/10.1208/s12248-011-9303-8.

[32] T. Weng, W. Zhang, Y. Xia, P. Wu, M. Yang, R. Jin, S. Xia, J. Wang, C. You, C. Han, X. Wang, 3D bioprinting for skin tissue engineering: current status and perspectives, J. Tissue Eng. 12 (2021) 1–28, https://doi.org/10.1177/20417314211028574.

[33] H. Zhao, J. Xu, H. Yuan, E. Zhang, N. Dai, Z. Gao, Y. Huang, F. Lv, L. Liu, Q. Gu, S. Wang, 3D printing of artificial skin patches with bioactive and optically active polymer materials for anti-infection and augmenting wound repair, Mater. Horiz. 9 (2022) 342–349, https://doi.org/10.1039/d1mh00508a.

[34] A. Georgopoulou, S. Lee, B. Dai, F. Bono, J. Hughes, E. Amstad, 3D printing of self-healing longevous multi-sensory e-skin, Commun. Mater. 6 (2025) 121, https://doi.org/10.1038/s43246-025-00839-7.

[35] R. Eugster, A.A. Ganguin, A. Seidi, S. Aleandri, P. Luciani, 3D printing injectable microbeads using a composite liposomal ink for local treatment of peritoneal diseases, drug Deliv, Transl. Res. 14 (2023) 1567–1581, https://doi.org/10.1007/s13346-023-01472-y.

[36] H. Peng, B. Han, T. Tong, X. Jin, Y. Peng, M. Guo, B. Li, J. Ding, Q. Kong, Q. Wang, 3D printing processes in precise drug delivery for personalized medicine, Biofabrication 16 (2024) 032001, https://doi.org/10.1088/1758-5090/ad3a14.

[37] C. Dong, M. Petrovic, I.J. Davies, Applications of 3D printing in medicine: A review, Ann 3D, Print Med 14 (2024) 100149, https://doi.org/10.1016/j.stlm.2024.100149.

[38] M. Carone, R. Gazzi, R. Eugster, R. Gelli, N. Manten, A.A. Ganguin, S. Di Valerio, G. Yadav, P. Castaldo, R. Mezzenga, P. Luciani, S. Aleandri, 3D-printed lipid mesophases for the treatment of chronic liver disease, Adv. Mater. Technol. 9 (2024) 2301930, https://doi.org/10.1002/admt.202301930.

[39] R. Eugster, M. Santschi, G. Buttitta, B. Olcay, J.L. Reymond, S. Aleandri, P. Luciani, 3D-printed cannabidiol stent for local treatment of urinary tract infections, Int. J. Pharm. 680 (2025) 125761, https://doi.org/10.1016/j.ijpharm.2025.125761.

[40] A. Abbadessa, P. Nuñez Bernal, G. Buttitta, A. Ronca, U. D'Amora, C. Zihlmann, N. Stiefel, L. Ambrosio, J. Malda, R. Levato, J. Crecente-Campo, M.J. Alonso, Biofunctionalization of 3D printed collagen with bevacizumab-loaded microparticles targeting pathological angiogenesis, J. Control. Release 360 (2023) 747–758, https://doi.org/10.1016/j.jconrel.2023.07.017.

[41] Y. Wang, X. Yuan, B. Yao, S. Zhu, P. Zhu, S. Huang, Tailoring bioinks of extrusion-based bioprinting for cutaneous wound healing, Bioact. Mater. 17 (2022) 178–194, https://doi.org/10.1016/j.bioactmat.2022.01.024.

[42] S.J. Lee, J.H. Lee, J. Park, W.D. Kim, S.A. Park, Fabrication of 3D printing scaffold with porcine skin decellularized bio-ink for soft tissue engineering, Materials 13 (2020), https://doi.org/10.3390/MA13163522.

[43] T. Mohan, M. Bračič, D. Bračič, F. Lackner, C. Nagaraj, A.D. Štiglic, R. Kargl, K. S. Kleinschek, Protocol for the fabrication of self-standing (nano)cellulose-based 3D scaffolds for tissue engineering, STAR Protoc 6 (2025) 103583, https://doi.org/10.1016/j.xpro.2024.103583.

[44] S.J. Lee, J.H. Lee, J. Park, W.D. Kim, S.A. Park, Fabrication of 3D printing scaffold with porcine skin decellularized bio-ink for soft tissue engineering, Materials 13 (2020) 3522, https://doi.org/10.3390/MA13163522.

[45] M.T. Wolf, K.A. Daly, E.P. Brennan-Pierce, S.A. Johnson, C.A. Carruthers, A. D'Amore, S.P. Nagarkar, S.S. Velankar, S.F. Badylak, A hydrogel derived from decellularized dermal extracellular matrix, Biomaterials 33 (2012) 7028–7038, https://doi.org/10.1016/j.biomaterials.2012.06.051.

[46] S.N. Politis, P. Colombo, G. Colombo, D.M. Rekkas, Design of experiments (DoE) in pharmaceutical development, Drug Dev. Ind. Pharm. 43 (2017) 889–901, https://doi.org/10.1080/03639045.2017.1291672.

[47] G. Buttitta, S. Bonacorsi, C. Barbarito, M. Moliterno, S. Pompei, G. Saito, I. Oddone, G. Verdone, D. Secci, S. Raimondi, Scalable microfluidic method for tunable liposomal production by a design of experiment approach, Int. J. Pharm. 662 (2024) 124460, https://doi.org/10.1016/j.ijpharm.2024.124460.

[48] F. Weber, D.C. Ivan, S.T. Proulx, G. Locatelli, S. Aleandri, P. Luciani, Beyond trial and error: A systematic development of liposomes targeting primary macrophages, Adv. Nanobiomed Res. 1 (2021) 2000098, https://doi.org/10.1002/anbr.202000098.

[49] E. Jo Jang, R. Patel, N.V. Sankpal, L.S. Bouchard, M. Patel, Alginate, hyaluronic acid, and chitosan-based 3D printing hydrogel for cartilage tissue regeneration, Eur. Polym. J. 202 (2024) 112651, https://doi.org/10.1016/j.eurpolymj.2023.112651.

[50] Y. Cui, F. Yang, C.S. Wang, A. Blennow, C. Li, X. Liu, 3D printing windows and rheological properties for normal maize starch/sodium alginate composite gels, Food Hydrocoll. 146 (2024) 109178, https://doi.org/10.1016/j.foodhyd.2023.109178.

[51] N. Farshidfar, S. Iravani, R.S. Varma, Alginate-based biomaterials in tissue engineering and regenerative medicine, Mar. Drugs 21 (2023) 1–17, https://doi.org/10.3390/md21030189.

[52] Y. Cheng, X. Shi, X. Jiang, X. Wang, H. Qin, Printability of a cellulose derivative for extrusion-based 3D printing: the application on a biodegradable support material, Front. Mater. 7 (2020), https://doi.org/10.3389/fmats.2020.00086.

[53] P. Polamaplly, Y. Cheng, X. Shi, K. Manikandan, G.E. Kremer, H. Qin, 3D Printing and characterization of hydroxypropyl methylcellulose and methylcellulose for biodegradable support structures, Procedia Manuf. 34 (2019) 552–559, https://doi.org/10.1016/j.promfg.2019.06.219.

[54] S. Teworte, S. Aleandri, J.R. Weber, M. Carone, P. Luciani, Mucoadhesive 3D printed vaginal ovules to treat endometriosis and fibrotic uterine diseases, Eur. J. Pharm. Sci. 188 (2023) 106501, https://doi.org/10.1016/j.ejps.2023.106501.

[55] Y. Wang, A. Otte, H. Park, K. Park, In vitro-in vivo correlation (IVIVC) development for long-acting injectable drug products based on poly(lactide-co-glycolide), J. Control. Release 377 (2025) 186–196, https://doi.org/10.1016/j.jconrel.2024.11.021.

[56] J. Kumari, S. Pandey, K.K. Jangde, P.V. Kumar, D.K. Mishra, Evolution, integration, and challenges of 3D printing in pharmaceutical applications: A comprehensive review, Bioprinting 44 (2024) e00367, https://doi.org/10.1016/j.bprint.2024.e00367.

[57] L. Menon, D. Sanjanwala, S. Sharma, R. Parul, P. Dandekar Jain, Sterilizing bioinks: understanding the impact of techniques on 3D bioprinting materials, Bioprinting 48 (2025) e00399, https://doi.org/10.1016/j.bprint.2025.e00399.

[58] J. Kožák, M. Rabišková, A. Lamprecht, In-vitro drug release testing of parenteral formulations via an agarose gel envelope to closer mimic tissue firmness, Int. J. Pharm. 594 (2021) 120142, https://doi.org/10.1016/j.ijpharm.2020.120142.

[59] D.H. Leung, Y. Kapoor, C. Alleyne, E. Walsh, A. Leithead, B. Habulihaz, G. M. Salituro, A. Bak, T. Rhodes, Development of a convenient in vitro gel diffusion model for predicting the in vivo performance of subcutaneous parenteral formulations of large and small molecules, AAPS PharmSciTech 18 (2017) 2203–2213, https://doi.org/10.1208/s12249-016-0698-5.

[60] C. Bassand, L. Benabed, J. Freitag, J. Verin, F. Siepmann, J. Siepmann, How bulk fluid renewal can affect in vitro drug release from PLGA implants: importance of the experimental set-up, Int J Pharm X 4 (2022) 100131, https://doi.org/10.1016/j.ijpx.2022.100131.

[61] C.D. Bruno, J.S. Harmatz, S.X. Duan, Q. Zhang, C.R. Chow, D.J. Greenblatt, Effect of lipophilicity on drug distribution and elimination: influence of obesity, Br. J. Clin. Pharmacol. 87 (2021) 3197–3205, https://doi.org/10.1111/bcp.14735.

[62] C.M. Deadman, I.W. Kellaway, M. Yasin, P.A. Dickinson, S. Murdan, An investigation into the influence of drug lipophilicity on the in vivo absorption profiles from subcutaneous microspheres and in situ forming depots, J. Control. Release 122 (2007) 79–85, https://doi.org/10.1016/j.jconrel.2007.06.013.

[63] A. Glasenapp, J.P. Bankstahl, H. Bähre, A. Kozlov, S. Glage, M. Bankstahl, Favorable pharmacokinetic and tolerability profiles make carprofen an attractive analgesic for subcutaneous injection and oral self-administration in rats, Sci. Rep. 15 (2025) 8932, https://doi.org/10.1038/s41598-025-93336-3.

[64] H. Lou, M.J. Hageman, Development of an in vitro system to emulate an in vivo subcutaneous environment: small molecule drug assessment, Mol. Pharm. 19 (2022) 4017–4025, https://doi.org/10.1021/acs.molpharmaceut.2c00490.

[65] C. Bassand, J. Verin, M. Lamatsch, F. Siepmann, J. Siepmann, How agarose gels surrounding PLGA implants limit swelling and slow down drug release, J. Control. Release 343 (2022) 255–266, https://doi.org/10.1016/j.jconrel.2022.01.028.

[66] K. Peynshaert, J. Devoldere, S.C. De Smedt, K. Remaut, In vitro and ex vivo models to study drug delivery barriers in the posterior segment of the eye, Adv. Drug Deliv. Rev. 126 (2018) 44–57, https://doi.org/10.1016/j.addr.2017.09.007.

[67] R. Eugster, M. Orsi, G. Buttitta, N. Serafini, M. Tiboni, L. Casettari, J.-L. Reymond, S. Aleandri, P. Luciani, Leveraging machine learning to streamline the development of liposomal drug delivery systems, J. Control. Release 376 (2024) 1025–1038, https://doi.org/10.1016/j.jconrel.2024.10.065.

[68] G. Buttitta, L. Lavagna, S. Bonacorsi, C. Barbarito, M. Moliterno, G. Saito, I. Oddone, G. Verdone, S. Raimondi, M. Panella, Machine learning-guided microfluidic optimization of clinically inspired liposomes for nanomedicine applications, Int. J. Pharm. 686 (2025), https://doi.org/10.1016/j.ijpharm.2025.126362.

[69] L. Carbone, Estimating mouse and rat use in American laboratories by extrapolation from animal welfare act-regulated species, Sci. Rep. 11 (2021) 493, https://doi.org/10.1038/s41598-020-79961-0.

[70] J.H. Kim, D.W. Kang, G.W. Choi, S.B. Lee, S. Lee, H.Y. Cho, Evaluation of lidocaine and metabolite pharmacokinetics in hyaluronic acid injection, Pharmaceutics 13 (2021) 1–16, https://doi.org/10.3390/pharmaceutics13020203.

[71] R.F. Grace, S.R. Edwards, L.E. Mather, Y. Lin, I. Power, Central and peripheral tissue distribution of diclofenac after subcutaneous injection in the rat, Inflammopharmacology 8 (2000) 43–54.

[72] Y. Jiao, J. Yan, D.S. Sutaria, P. Lu, M. Vicchiarelli, Z. Reyna, J. Ruiz-Delgado, E. Burk, E. Moon, N.R. Shah, B. Spellberg, R.A. Bonomo, G.L. Drusano, A. Louie, B.M. Luna, J.B. Bulitta, Population pharmacokinetics and humanized dosage regimens matching the peak, area, trough, and range of amikacin plasma concentrations in immune-competent murine bloodstream and lung infection models, Antimicrob. Agents Chemother. 68 (2024) 01394, https://doi.org/10.1128/aac.01394-23.

[73] P.C. Chiang, K. Nagapudi, P.W. Fan, J. Liu, Investigation of drug delivery in rats via subcutaneous injection: case study of pharmacokinetic Modeling of suspension formulations, J. Pharm. Sci. 108 (2019) 109–119, https://doi.org/10.1016/j.xphs.2018.06.003.

[74] G.S. Prins, S.H. Ye, L. Birch, S. Mei Ho, K. Kannan, Serum bisphenol A pharmacokinetics and prostate neoplastic responses following oral and subcutaneous exposures in neonatal Sprague-Dawley rats, Reprod. Toxicol. 31 (2011) 1–9, https://doi.org/10.1016/j.reprotox.2010.09.009.

[75] A. Bernareggi, A. Danese, L. Cavenaghi, B.P. Goldstein, E. Selva, L. Gastaldo, M. Berti, R. Pallanza, F. Ripamonti, P. Ferrari, M. Denaro, V. Arioli, G. Cassani, A., Agents Chemother, pharmacokinetics of A40926 in rats after single intravenous and subcutaneous doses A40926 is a new glycopeptide antibiotic with unique activity against Neisseria gonorrhoeae and high and prolonged levels in mouse blood, Antimicrob. Agents Chemother. 32 (1988) 246–249. https://journals.asm.org/journal/aac.

[76] L. Laurén, T. Österman, T. Karhi, Pharmacokinetics of clodronate after single intravenous, intramuscular and subcutaneous injections in rats, Pharmacol. Toxicol. 69 (1991) 365–368, https://doi.org/10.1111/j.1600-0773.1991.tb01312.x.

[77] M.S.S. Bergh, I.L. Bogen, N. Garibay, M.H. Baumann, Pharmacokinetics and pharmacodynamics of cyclopropylfentanyl in male rats, Psychopharmacology 238 (2021) 3629–3641, https://doi.org/10.1007/s00213-021-05981-x.

[78] A. Sandberg, K.S. Jensen, P. Baudoux, F. Van Bambeke, P.M. Tulkens, N. Frimodt-Møller, Intra- and extracellular activities of dicloxacillin against Staphylococcus aureus in vivo and in vitro, Antimicrob. Agents Chemother. 54 (2010) 2391–2400, https://doi.org/10.1128/AAC.01400-09.

[79] A. Glasenapp, J.P. Bankstahl, H. Bähre, S. Glage, M. Bankstahl, Subcutaneous and orally self-administered high-dose carprofen shows favorable pharmacokinetic and tolerability profiles in male and female C57BL/6J mice, Front. Vet. Sci. 11 (2024) 1430726, https://doi.org/10.3389/fvets.2024.1430726.

[80] S.H. Jeong, J.H. Jang, Y.B. Lee, Pharmacokinetic comparison of three different administration routes for topotecan hydrochloride in rats, Pharmaceuticals 13 (2020) 1–16, https://doi.org/10.3390/ph13090231.

[81] Z. Li, J. Zhang, X. Li, X. Guo, Z. Zhang, Preparation and evaluation of multifunctional autofluorescent magnetic nanoparticle–based drug delivery systems against mammary cancer, J. Pharm. Sci. 107 (2018) 2694–2701, https://doi.org/10.1016/j.xphs.2018.06.009.

[82] X. Liu, Q. Yang, Y. Fan, Y. Du, L. Lei, D. Wang, Y. Liu, Pharmacokinetics and pharmacodynamics of enrofloxacin treatment of Escherichia coli in a murine thigh infection modeling, BMC Vet. Res. 17 (2021) 212, https://doi.org/10.1186/s12917-021-02908-8.

[83] S. Han, C. Liu, H. Chen, Y. Fu, Y. Zhang, R. Miao, P. Ren, P. Yu, Z. Shi, Y. Tian, H. Wang, T. Liu, H. Hou, Q. Hu, Pharmacokinetics of freebase nicotine and nicotine salts following subcutaneous administration in male rats, Drug Test Anal. 15 (2023) 1099–1106, https://doi.org/10.1002/dta.3363.

[84] P.C. Chiang, K. Nagapudi, P.W. Fan, J. Liu, Investigation of drug delivery in rats via subcutaneous injection: case study of pharmacokinetic Modeling of suspension formulations, J. Pharm. Sci. 108 (2019) 109–119, https://doi.org/10.1016/j.xphs.2018.06.003.

[85] J.S. Elmore, O. Dillon-Carter, J.S. Partilla, K.N. Ellefsen, M. Concheiro, M. Suzuki, K.C. Rice, M.A. Huestis, M.H. Baumann, Pharmacokinetic profiles and pharmacodynamic effects for methylone and its metabolites in rats, Neuropsychopharmacology 42 (2017) 649–660, https://doi.org/10.1038/npp.2016.213.

[86] C.E. Lau, M.Y. Fang, C. Wang, C.E. Smith, F. Lau, Y. Ma, Wang, pharmacokinetics and bioavailability of midazolam after intravenous, subcutaneous, intraperitoneal and oral administration under a chronic food-limited regimen: relating DRL performance to pharmacokinetics, Psychopharmacology 126 (1996) 241–248.

[87] J.R. Canfield, J.E. Sprague, In vivo pharmacokinetic, pharmacodynamic and brain concentration comparison of fentanyl and Para-fluorofentanyl in rats, Arch. Toxicol. 99 (2025) 287–297, https://doi.org/10.1007/s00204-024-03887-z.

[88] L.T. Kint, B.J. Seewoo, T.H. Hyndman, M.W. Clarke, S.H. Edwards, J. Rodger, K. W. Feindel, G.C. Musk, The pharmacokinetics of medetomidine administered subcutaneously during isoflurane anaesthesia in Sprague-dawley rats, Animals 10 (2020) 1–14, https://doi.org/10.3390/ani10061050.

[89] L. Kendall, R. Hansen, K. Dorsey, S. Kang, P. Lunghofer, D. Gustafson, Pharmacokinetics of sustained release analgesics in mice, J. Am. Assoc. Lab. Anim. Sci. 53 (2014) 78–484.

[90] E.J. De Waal, H. Schuurman, C. Hendriksen, B. Elvers, A. Van Dijk, H. Van Loveren, Effects of subcutaneous versus intravenous administration of cyclosporin A on rat thymic histology and pharmacokinetics, Int. J. Immunopharmacol. 14 (1992) 1101–1105.

[91] X. Li, D.C. Dubois, R.R. Almon, W.J. Jusko, Physiologically based pharmacokinetic modeling involving nonlinear plasma and tissue binding: application to prednisolone and prednisone in rats, J. Pharmacol. Exp. Ther. 375 (2020) 385–396, https://doi.org/10.1124/JPET.120.000191.

[92] R. Evangelista Vaz, D.I. Draganov, C. Rapp, F. Avenel, G. Steiner, M. Arras, A. Bergadano, Preliminary pharmacokinetics of tramadol hydrochloride after administration via different routes in male and female B6 mice, Vet. Anaesth. Analg. 45 (2018) 111–122, https://doi.org/10.1016/j.vaa.2016.09.007.

[93] J.R. Canfield, D.F. Kisor, J.E. Sprague, Designer benzodiazepine rat pharmacokinetics: A comparison of alprazolam, flualprazolam and flubromazolam, Toxicol. Appl. Pharmacol. 465 (2023) 116459, https://doi.org/10.1016/j.taap.2023.116459.

[94] M.K. Reinhard, I. Bekersky, T.W. Sanders, B.J. Harris, G.H. Hotlendorf, Effects of Polyaspartic acid on pharmacokinetics of tobramycin in two strains of rat, Antimicrob. Agents Chemother. 38 (1994) 79–82, https://journals.asm.org/journal/aac.

[95] D. Song, L. Sun, D.C. DuBois, R.R. Almon, S. Meng, W.J. Jusko, Physiologically based pharmacokinetics of dexamethasone in rats, Drug Metab. Dispos. 48 (2020) 811–818, https://doi.org/10.1124/dmd.120.091017.

[96] F. Gaudette, A. Hamadjida, D. Bédard, S.G. Nuara, F. Beaudry, P. Huot, Development and validation of a high-performance liquid chromatography-tandem mass spectrometry method to quantify LY-354,740 in rat and marmoset plasma, J. Chromatogr. B Anal. Technol. Biomed. Life Sci. 1061–1062 (2017) 392–398, https://doi.org/10.1016/j.jchromb.2017.07.007.

[97] K. Matsumoto, Y. Kurihara, Y. Kuroda, S. Hori, J. Kizu, Pharmacokinetics and brain penetration of carbapenems in mice, J. Infect. Chemother. 22 (2016) 346–349, https://doi.org/10.1016/j.jiac.2015.11.010.

[98] M. Le Nedelec, P. Glue, H. Winter, C. Goulton, N.J. Medlicott, The effect of route of administration on the enantioselective pharmacokinetics of ketamine and norketamine in rats, J. Psychopharmacol. 32 (2018) 1127–1132, https://doi.org/10.1177/0269881118780013.

[99] K. Sanders, E. Bas, S. Cox, D. Rothen, Pharmacokinetics of single-bolus subcutaneous cefovecin in C57BL/6 mice, J. Am. Assoc. Lab. Anim. Sci. 56 (2017) 558–561, https://vetlabel.com/.

[100] S.S. Lewis, L.C. Loram, M.R. Hutchinson, C.M. Li, Y. Zhang, S.F. Maier, Y. Huang, K.C. Rice, L.R. Watkins, (+)-naloxone, an opioid-inactive toll-like receptor 4 signaling inhibitor, reverses multiple models of chronic neuropathic pain in rats, J. Pain 13 (2012) 498–506, https://doi.org/10.1016/j.jpain.2012.02.005.

[101] P.K.F. Yeung, A. Alcos, J. Tang, B. Tsui, Pharmacokinetics and metabolism of diltiazem in rats: comparing single vs repeated subcutaneous injections in vivo, Biopharm. Drug Dispos. 28 (2007) 403–407, https://doi.org/10.1002/bdd.568.

[102] T. Páleníček, M. Balíková, V. Bubeníková-Valešová, J. Horáček, Mescaline effects on rat behavior and its time profile in serum and brain tissue after a single subcutaneous dose, Psychopharmacology 196 (2008) 51–62, https://doi.org/10.1007/s00213-007-0926-5.

[103] K. Beránková, M. Szkutová, M. Balíková, Distribution profile of 2,5-dimethoxy-4-bromoamphetamine (DOB) in rats after oral and subcutaneous doses, Forensic Sci. Int. 170 (2007) 94–99, https://doi.org/10.1016/j.forsciint.2007.03.023.

[104] B. Kick, P. Shu, B. Wen, D. Sun, D. Taylor, Pharmacokinetic profiles of nalbuphine after intraperitoneal and subcutaneous administration to C57BL/6 mice, J. Am. Assoc. Lab. Anim. Sci. 56 (2017) 534–538.

[105] P.H. Chen, K.L. Boyd, E.K. Fickle, C.W. Locuson, Subcutaneous meloxicam suspension pharmacokinetics in mice and dose considerations for postoperative analgesia, J. Vet. Pharmacol. Ther. 39 (2016) 356–362, https://doi.org/10.1111/jvp.12297.

[106] C.E. Lau, L. Sun, Q. Wang, J.L. Falk, C.E. Lau, The effect of zolpidem on operant behavior and its relation to pharmacokinetics after intravenous and subcutaneous administration: concentration-effect relations, Behav. Pharmacol. 13 (2002) 93–103.

[107] R. Guilhaumou, A. Boulamery, B. Deluca, E. Deturmeny, B. Bruguerolle, Effects of induced hyperthermia on pharmacokinetics of ropivacaine in rats, Fundam. Clin. Pharmacol. 24 (2010) 463–468, https://doi.org/10.1111/j.1472-8206.2009.00803.x.

[108] Y. Zhang, M. Huo, J. Zhou, S. Xie, PKSolver: an add-in program for pharmacokinetic and pharmacodynamic data analysis in Microsoft excel, Comput. Methods Prog. Biomed. 99 (2010) 306–314, https://doi.org/10.1016/j.cmpb.2010.01.007.

[109] M. Orsi, S. Loh, W. Cheng, H. Ang, A. Frei, Using machine learning to predict the antibacterial activity of ruthenium complexes**, Angew. Chem. Int. Ed. 63 (2023) e202317901, https://doi.org/10.26434/chemrxiv-2023-72srv-v2.

[110] S. Tretiakov, A.K. Nigam, R. Pollice, Studying noncovalent interactions in molecular systems with machine learning, Chem. Rev. 125 (2025) 5776–5829, https://doi.org/10.1021/acs.chemrev.4c00893.

[111] S. Lundberg, S.-I. Lee, A Unified Approach to Interpreting Model Predictions, Long Beach. https://github.com/slundberg/shap, 2017.

[112] J. Jiménez-Luna, F. Grisoni, G. Schneider, Drug discovery with explainable artificial intelligence, Nat Mach Intell 2 (2020) 573–584, https://doi.org/10.1038/s42256-020-00236-4.

[113] S.M. Lundberg, G. Erion, H. Chen, A. DeGrave, J.M. Prutkin, B. Nair, R. Katz, J. Himmelfarb, N. Bansal, S.I. Lee, From local explanations to global understanding with explainable AI for trees, Nat Mach Intell 2 (2020) 56–67, https://doi.org/10.1038/s42256-019-0138-9.

[114] I. Roshanski, M. Kalech, L. Rokach, Automatic feature engineering for learning compact decision trees, Expert Syst. Appl. 229 (2023) 120470, https://doi.org/10.1016/j.eswa.2023.120470.

[115] K.A. Einarson, K.M. Bendtsen, K. Li, M. Thomsen, N.R. Kristensen, O. Winther, S. Fulle, L. Clemmensen, H.H.F. Refsgaard, Molecular representations in machine-learning-based prediction of PK parameters for insulin Analogs, ACS Omega 8 (2023) 23566–23578, https://doi.org/10.1021/acsomega.3c01218.

[116] M.V.S. Varma, B. Feng, R.S. Obach, M.D. Troutman, J. Chupka, H.R. Miller, A. El-Kattan, Physicochemical determinants of human renal clearance, J. Med. Chem. 52 (2009) 4844–4852, https://doi.org/10.1021/jm900403j.

[117] N. Kaboudi, A. Shayanfar, Predicting the drug clearance pathway with structural descriptors, Eur. J. Drug Metab. Pharmacokinet. 47 (2022) 363–369, https://doi.org/10.1007/s13318-021-00748-3.

[118] H. Möbitz, Design principles for balancing lipophilicity and permeability in beyond rule of 5 space, ChemMedChem 19 (2024) e202300395, https://doi.org/10.1002/cmdc.202300395.

[119] R. Gomeni, F. Bressolle-Gomeni, Modeling complex pharmacokinetics of long-acting injectable products using convolution-based models with nonparametric input functions, J. Clin. Pharmacol. 61 (2021) 1081–1095, https://doi.org/10.1002/jcph.1842.

[120] N.S. Chumbler, J.C. Schildt, D.I. Mawby, M.G. Papich, Use of intravenous lipid therapy in a cat with carprofen overdose, Clin. Case Reports 8 (2020) 653–657, https://doi.org/10.1002/ccr3.2772.

[121] R. Eugster, P. Luciani, Liposomes: bridging the gap from lab to pharmaceuticals, Curr. Opin. Colloid Interface Sci. 75 (2025) 101875, https://doi.org/10.1016/j.cocis.2024.101875.

[122] H. Koppisetti, S. Abdella, D.D. Nakmode, F. Abid, F. Afinjuomo, S. Kim, Y. Song, S. Garg, Unveiling the future: opportunities in long-acting injectable drug development for veterinary care, Pharmaceutics 17 (2025) 626, https://doi.org/10.3390/pharmaceutics17050626.

[123] R.T. Coones, I. Nikolic, R. Eugster, D. Mehn, V. Tong, P. Luciani, C. Minelli, Best practice for the size analysis of nanomedicines – an iron sucrose case study, Int. J. Pharm. 674 (2025) 125452, https://doi.org/10.1016/j.ijpharm.2025.125452.